

CERN 76-04
SPS Division
8 March 1976

ORGANISATION EUROPÉENNE POUR LA RECHERCHE NUCLÉAIRE
CERN EUROPEAN ORGANIZATION FOR NUCLEAR RESEARCH

THE RADIATION ENVIRONMENT OF PROTON ACCELERATORS
AND STORAGE RINGS

G.R. Stevenson

G E N E V A

1976

© Copyright CERN, Genève, 1976

Propriété littéraire et scientifique réservée pour tous les pays du monde. Ce document ne peut être reproduit ou traduit en tout ou en partie sans l'autorisation écrite du Directeur général du CERN, titulaire du droit d'auteur. Dans les cas appropriés, et s'il s'agit d'utiliser le document à des fins non commerciales, cette autorisation sera volontiers accordée.

Le CERN ne revendique pas la propriété des inventions brevetables et dessins ou modèles susceptibles de dépôt qui pourraient être décrits dans le présent document; ceux-ci peuvent être librement utilisés par les instituts de recherche, les industriels et autres intéressés. Cependant, le CERN se réserve le droit de s'opposer à toute revendication qu'un usager pourrait faire de la propriété scientifique ou industrielle de toute invention et tout dessin ou modèle décrits dans le présent document.

Literary and scientific copyrights reserved in all countries of the world. This report, or any part of it, may not be reprinted or translated without written permission of the copyright holder, the Director-General of CERN. However, permission will be freely granted for appropriate non-commercial use. If any patentable invention or registrable design is described in the report, CERN makes no claim to property rights in it but offers it for the free use of research institutions, manufacturers and others. CERN, however, may oppose any attempt by a user to claim any proprietary or patent rights in such inventions or designs as may be described in the present document.

CERN 76-04
SPS Division
8 March 1976

ORGANISATION EUROPÉENNE POUR LA RECHERCHE NUCLÉAIRE
CERN EUROPEAN ORGANIZATION FOR NUCLEAR RESEARCH

THE RADIATION ENVIRONMENT OF PROTON ACCELERATORS
AND STORAGE RINGS

G.R. Stevenson

G E N E V A

1976

ABSTRACT

These lecture notes survey the physical processes that give rise to the stray-radiation environment of proton synchrotrons and storage rings, with emphasis on their importance for radiation protection. The origins of the prompt radiation field (which disappears when the accelerator is switched off) are described in some detail: proton-nucleus interactions, extranuclear cascades, muon generation and transport. The effects of induced radioactivity in the accelerator structure and surroundings, notably in iron, concrete, air, and water, are discussed and methods for monitoring hadrons in the radiation environment outside the accelerator are listed. Seventy-six references to the literature are included.

CONTENTS

	<u>Page</u>
1. INTRODUCTION	1
2. RADIATION ENVIRONMENT	1
3. PROTON NUCLEUS INTERACTION	2
3.1 The primary process	3
3.2 The cascade	7
3.3 The return to equilibrium	8
4. THE EXTRANUCLEAR CASCADE	10
5. THE PROMPT FIELD CLOSE TO THE ACCELERATOR	16
6. THE SHIELDED HADRON COMPONENT	18
7. THE DIRECT MUON COMPONENT	21
7.1 Probability of decay	23
7.2 Decay kinematics	24
7.3 Momentum distribution	25
7.4 Cascade muons	26
7.5 Muon scattering	26
8. RADIATION ESCAPING FROM TUNNELS AND DUCTS	27
9. SKYSHINE (AIR-SCATTERED RADIATION)	28
10. INDUCED RADIOACTIVITY -- ACCELERATOR STRUCTURE	29
11. ACTIVATION OF ELEMENTS OTHER THAN IRON	31
12. ACTIVATION OF CONCRETE	32
13. INDUCED ACTIVITY -- AIR AND WATER	34
14. PROTON SYNCHROTRONS VERSUS STORAGE RINGS	34
15. REMAINING PROBLEMS	35
REFERENCES	37
FIGURES	40

1. INTRODUCTION

This paper is based on a lecture given as part of a course on High-Energy Radiation Dosimetry and Protection, at Erice (Sicily), in October 1975. It aims to give a physical description of the radiation field around proton accelerators and storage rings, laying particular emphasis on its origins and on the components of importance for radiation protection.

2. RADIATION ENVIRONMENT

There are three distinct and separate radiation fields:

- i) Prompt - directly associated in time with the operation of the accelerator, i.e. it disappears when the accelerator is switched off.

There are two types of spectra: a) direct and
b) scattered.

- ii) Remanent - remains after the accelerator has been switched off; it is due to radioactivity in the accelerator structure.
- iii) Pseudo prompt - occurs when injection to accelerator is off but certain high voltages or RF generators are on, e.g. ejection septum or separator conditioning.

This last hazard is simply due to X-rays, and for shielding we can use the classical ICRP curves¹⁾ if we know the mean current. Since it is an intermittent hazard it is difficult to design adequate shielding that is always safe but not cumbersome. At least 90% of dose accumulated by personnel comes from (ii), i.e. from purely conventional X, γ , and β radiation fields.

We must be careful *not to over-dramatize* the prompt radiation field, even though for a physicist it may be the most intellectually satisfying to investigate. Often it is shielded out of importance and does not form a major part of the dose commitment.

The radiation environment is governed by the beam loss distribution; losses can occur during some or all of the following phases:

<u>Proton synchrotron</u>	<u>Storage ring</u>
pre-acceleration	transfer
injection	(scraping)
transition	injection
(scraping)	(scraping)
ejection	coasting
(scraping)	(scraping)
targetting	dumping
dumping.	

Thus hazards (i) and (ii) all start with the proton-nucleus inelastic interaction.

3. PROTON NUCLEUS INTERACTION

The best visualization of a proton-nucleus interaction is given by the "stars" in nuclear emulsions exposed either to cosmic radiation at high altitudes or to proton beams. The visible tracks of particles originating from the star fall into three categories:

- i) minimum ionizing tracks of shower particles: identified as protons, pions, kaons with energies > 600 MeV;
- ii) grey tracks: shower protons with some π mesons and deuterons having energies between 25-500 MeV;
- iii) black tracks: low-energy protons, deuterons, tritons, α particles, and sometimes heavier fragments.

In fact at least 30 different types of short-lived fundamental particles can be created. Most have lifetimes of $< 10^{-12}$ sec and decay into nucleons and/or the more common types of mesons. Those which concern us from the point of view of the radiation environment are shown in the schematic extra-nuclear cascade illustrated in Fig. 1²⁾. But we should return to the details of the basic inelastic interaction.

The collision of a fast particle with a nucleus is considered in four stages:

- i) the interaction of the incident particle with an individual nucleon of the target nucleus;
- ii) the cascade stage -- the successive collisions of the initial collision products + descendants with the target nucleons;
- iii) the evaporation stage which results in a nucleus which is stable against further evaporation of nucleons or clusters of nucleons;
- iv) radioactive decay -- the nucleus transforms via α or β decay to another nucleus which is closer to the stability line; but this will concern us later.

3.1 The primary process

When the particle wavelength λ is less than the spacing between nucleons, the collision approaches that of a free particle-nucleon collision; i.e.

$$\lambda = \frac{h \text{ (GeV sec)} \times c}{p \text{ (GeV/c)}} < \text{a few} \times 10^{-14} \text{ cm}$$

or

$$p > \frac{4.1 \times 10^{-24} \times 3 \times 10^{10}}{3 \times 10^{-14}} \sim \text{a few GeV/c} ,$$

where h is Planck's constant and p is the particle momentum.

However, even at energies of ~ 200 MeV it is still possible to resolve the shell structure in a proton-light nucleus collision³⁾.

The state of theoretical models of multiple-meson production in p-p, p-n, or p-nucleus collisions as of 1962 is summarized by Ramakrishnan⁴⁾ in a way which is not too detailed for the non-expert. More recent theories are summarized by G. Ranft and J. Ranft⁵⁾ and in other reviews in the Rochester Conference series. The power of the thermodynamical model (fireballs) of Hagedorn, Ranft and others is illustrated in Ref. 6, where the theory is summarized and many comparisons made between the theory and experimental data. Two examples from this report are given in Figs. 2 and 3.

However, for Monte Carlo calculations of the hadron cascade we need simple formulae which allow an efficient selection of random secondary particle momenta and angles and which describe the secondary particle spectra as well as possible. The first, used widely for this purpose, was the CKP formula⁷⁾. For pions:

$$\frac{d^2N}{dpd\Omega} = \frac{n E}{2\pi p_0^2 T} \exp \left[-E \left(\frac{1}{T} + \frac{\theta}{p_0} \right) \right],$$

where

E is the energy of the secondary pion in GeV,

n is the pion multiplicity = $0.45 E_0^{1/4}$,

T is the mean pion energy = $0.20 E_0^{3/4}$,

E_0 is the primary proton energy,

p_0 characterizes the mean transverse momentum of the pions = 0.2.

Another is that due to Trilling⁸⁾, subsequently modified by Ranft⁹⁾ and Ranft and Borak¹⁰⁾. The formula for π^\pm , K^\pm , and \bar{p} production is

$$\begin{aligned} \frac{d^2N}{dpd\Omega} = & A_1 p^2 \exp \left(-A_2 \frac{p}{\sqrt{p_0}} - A_3 p \sqrt{p_0} \theta^2 \right) \\ & + A_4 \frac{p^2}{p_0} \exp \left[-A_5 \left(\frac{p}{p_0} \right)^2 - A_6 p \theta \right]. \end{aligned}$$

The parameters are given in Table 1. However, a more recent formula has been developed by Ranft¹¹⁾ which agrees with the predictions of the thermodynamical model and has the correct Feynman scaling behaviour. Unlike the previous two formulae which are described in the laboratory frame, the Ranft formula is described in the centre-of-mass frame.

Proton production is described by

$$\frac{d^2N}{dp_L^* dp_T} = \frac{A_1}{E_{cm}} \left(1 + \frac{A_2}{E_{cm}} p_L^* + \frac{A_3}{E_{cm}^2} p_L^{*2} \right) p_T \left[\exp(-A_4 p_T^2) + A_5 \exp(-A_6 p_T) \right],$$

where E_{cm} is the total c.m.s. energy (of p-p). The parameters are given in Table 2.

Table 1

Parameters for the Trilling production formula

Particle	Target	A ₁	A ₂	A ₃	A ₄	A ₅	A ₆
π^+	H ₂	1.65	4.8	2.6	3.12	10.4	3.9
π^-	H ₂	1.65	4.8	2.6	1.04	10.4	3.9
π^+	Be	1.67	3.76	4.23	1.76	10.21	4.28
π^-	Be	1.50	3.76	4.23	0.604	10.21	4.28
π^+	H ₂	3.386	4.146	4.556	7.141	9.600	4.823
π^-	H ₂	3.386	4.146	4.556	1.853	9.600	4.823
π^+	Be	3.52	4.15	4.56	3.49	9.87	4.04
π^-	Be	3.52	4.15	4.56	1.01	9.87	4.04
π^+	Al	3.88	4.15	4.56	3.04	10.0	3.91
π^-	Al	3.88	4.15	4.56	0.82	10.0	3.91
π^+	Cu	4.13	4.15	4.56	2.47	9.68	4.01
π^-	Cu	4.13	4.15	4.56	0.67	9.68	4.01
π^+	Pb	3.43	4.15	4.56	1.88	9.94	3.85
π^-	Pb	3.43	4.15	4.56	0.56	9.94	3.85
K ⁺	Be	0.0412	4.763	1.29	0.273	10.276	3.663
K ⁻	Be	0.0119	4.549	1.263	0.1046	18.187	3.259
\bar{p}	Be	0.008207	3.723	2.881	0.001846	11.104	5.156

Table 2

Parameters of the Ranft formula
describing proton production

Target	A ₁	A ₂	A ₃	A ₄	A ₅	A ₆
H ₂	8.71	0.86	-3.37	3.78	0.47	3.60
Be	2.65	1.03	-3.85	6.63	3.49	2.89
Al	2.76	-2.99	4.90	3.91	5.82	2.99
Cu	8.87	-1.78	0.30	5.38	0.38	1.41
Pb	3.10	1.01	-8.66	4.65	1.79	2.47

Pion production is described by

$$\frac{d^2 N^*}{dp_L^* dp_T} = \frac{A_1 \exp\left(-\frac{A_2}{E_{cm}^2} p_L^{*2}\right) p_T [\exp(-A_3 p_T^2) + A_4 \exp(-A_5 p_T)]}{(p_L^{*2} + p_T^2 + m_\pi^2)^{1/2}}$$

The parameters are given in Table 3.

Table 3

Parameters of the Ranft formula
describing pion production

Particle	Target	A ₁	A ₂	A ₃	A ₄	A ₅
π ⁺	H ₂	4.94	33.83	6.11	0.69	4.12
π ⁺	Be	1.81	33.39	3.01	5.12	7.34
π ⁺	Al	1.54	35.54	3.70	3.03	4.94
π ⁺	Cu	2.36	37.21	5.83	0.76	3.22
π ⁺	Pb	1.79	38.60	6.04	0.96	3.23
π ⁻	H ₂	2.81	44.08	5.17	0.81	4.34
π ⁻	Be	1.52	42.74	5.33	0.82	3.53
π ⁻	Al	1.54	44.62	5.67	0.83	3.17
π ⁻	Cu	1.60	46.52	6.47	0.93	3.05
π ⁻	Pb	1.55	47.16	6.02	0.50	2.66

These three models, plus a few more, are included in the Ranft computer program SPUKJ¹²⁾ for calculating and plotting single-particle spectra.

Various assumptions have to be used to obtain the remaining processes from the $p + N \rightarrow p$ and $p + N \rightarrow \pi^\pm$.

In his program FLUKA¹³⁾, Ranft assumed

1) for incident neutrons:

$$\begin{aligned} n + N \rightarrow p &\equiv p + N \rightarrow p \\ n + N \rightarrow \pi^\pm &\equiv p + N \rightarrow \pi^\pm \end{aligned}$$

2) for secondary neutron production:

$$p + N \rightarrow n \equiv p + N \rightarrow p$$

3) for incident pions:

$$\pi^\pm + N \rightarrow p \equiv \pi^\pm + N \rightarrow n \equiv \pi^\pm + N \rightarrow \pi^\pm \equiv p + N \rightarrow \pi^\pm .$$

However, in his later program KASPRO¹⁴⁾ the pion-induced reactions are more realistically represented.

The inelasticities, defined as $K_{ij}^0 = 1/E_i \int E_j (d^2N/dpd\Omega) dpd\Omega$, are:

<u>Incoming particle</u>	<u>Outgoing particle</u>			
	p	n	π^\pm	π^0
p	0.3	0.3	0.25	0.15
n	0.3	0.3	0.25	0.15
π^\pm	0.2	0.2	0.4	0.2

(Hyperons and kaons are assumed to be nucleons and pions.) Since a part of the energy is used for nuclear excitation (the fraction depending on the particle energy and target atomic weight), the above inelasticities are corrected:

$$K_{ij} = K_{ij}^0 \left(1 - \frac{E_{ex}}{E_0} \right).$$

Finally (or initially) we have the basic inelastic cross-section, which in Ranft's programs is interpolated from the following:

Material	H	Be	Al	Cu	Pb
σ_{abs} (mb)	31.5	227	472	850	1750

3.2 The cascade

The first collision with a nucleon in a complex nucleus is followed in rapid succession by further interactions of the collision partners and their descendants. Only large computer programs can hope to follow the development of such an intranuclear cascade in three dimensions. The first calculations were those of Metropolis et al.¹⁵⁾. Typically the attraction of nucleons for each other was represented by a square potential well with a depth of $\sim 30-40$ MeV. The Coulomb potential barrier is assumed to start at the nuclear radius of $1.3 \times 10^{-13} A^{1/3}$ but the exact shape strongly influences the emission at low energies. The early codes did not give good results above the energy threshold for pion production. This was remedied in the later versions of the intranuclear cascade programs of Bertini¹⁶⁾, where the nucleus is assumed to consist of a dense central core plus two annular regions whose density decreases with increasing radius. The single-particle potential for protons and neutrons

is taken to be $E_f + 7$ MeV, where E_f is the proton Fermi energy in the appropriate region. If, after a collision in the cascade, the energy of either particle is below the Fermi energy of that region, the collision is assumed to be forbidden, is ignored, and the nucleon allowed to proceed to the next interaction site. Extensive comparisons of the intranuclear cascade calculations with experimental data are given by Bertini, Guthrie and Culkowski¹⁷⁾. Two examples of the "goodness of fit" from this work are given in Figs. 4 and 5. At higher energies the increased multiplicity in nucleon-nucleon collisions gives rise to a significant depletion of nuclear material in the region of the cascade, with the result that the over-all cascade multiplicity does not rise as fast as predicted.

These effects will be taken into account in a new version of the code as foreseen by Gove, Bertini, Feliciano and Culkowski¹⁸⁾, whereby if a collision results in a new particle at the expense of nuclear matter, the density of the region in which the collision took place (and, if necessary, the surrounding region) is reduced by the equivalent of 1 mass unit. Nuclear matter then flows from one region to another if there is a density imbalance. Thus the developing cascade has to be followed in time as well as space. Recent experiments suggest that the multiplicity at very high energies (> 50 GeV) remains essentially constant.

3.3 The return to equilibrium

In the p-nucleus collision, the cascade traverses the nucleus in $\sim 10^{-22}$ sec. After the cascade the nucleus is somewhat excited. Initial theoretical investigations were made by Bohr¹⁹⁾, who reasoned that the strong forces between nucleons would facilitate the energy exchange between them so that the nucleus would quickly come to a "temperature equilibrium". Weisskopf²⁰⁾ applied statistical thermodynamics to the system to predict the emission of particles, but it was Frenkel²¹⁾ who first likened the process to one of evaporation.

The evaporation spectrum for each particle type can be given by Weisskopf's formula

$$N(E) dE \propto E e^{-E/\tau} dE ,$$

where τ is a so-called nuclear temperature with the dimensions of energy and is of the order of 2-10 MeV. The variation of τ with the energy of an incident proton or neutron is given in Ref. 15. The most probable energy for proton emission is in the region of several MeV.

The probability that a particle of mass m will be emitted per unit surface area of the excited nucleus/sec is

$$P(e) \propto \sum_s (2s + 1)m \exp\left(-\frac{mT}{10}\right) \exp\left(\frac{B + V^*}{T}\right).$$

The sum is taken over all s states of the nucleon; B is the binding energy of the particle to be emitted, V^* is the corrected Coulomb barrier height (to allow for penetration). These quantities vary, as shown in Table 4.

Table 4

Parameters for evaporation probability

Emitted particle	V^* (MeV)	B
n	0	8 + 74 x
p	0	8 - 110 x
d	4	14 - 37 x
t	5	16 + 37 x
^3He	5	16 - 148 x
^4He	10	4 - 74 x
^6Li	11	24 - 74 x
^8Be	20	8 - 148 x
^8B	25	29 - 330 x
Higher Z	5 Z	

The x is due to the fact that we do not have the most stable ratio of protons and neutrons,

$$x = \frac{Z - Z_s}{A}$$

where Z_s is the charge of the most stable species of the nucleus. The normalized probability of emission for two different temperatures is given in Table 5.

Table 5

Relative evaporation probabilities

Emitted particle	T = 3 MeV	T = 6 MeV
H	62	50
d	13	26
t	5	9
³ He	1	4
⁴ He	19	11
n	220	97
⁸ Li	0.02	0.17
n/(H+d+t)	2.4	1.5

Empirically it is found that

$$n/p = c(T) \exp \left[- \frac{1.4 (Z - Z_G)}{T} \right].$$

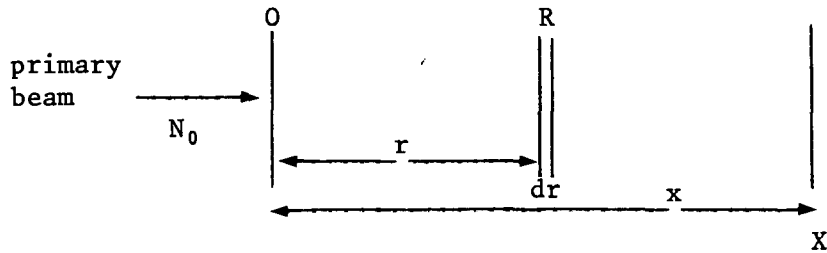
It should be remembered that in complete contrast to the particles created in the initial particle-nucleon collision and cascade processes, the distribution of particles in connection with nuclear evaporation is isotropic in the laboratory system.

4. THE EXTRANUCLEAR CASCADE

The development of the extranuclear cascade depends not only on the physics of the particle interactions but also on the configuration and composition of the materials in which the cascade develops. Analytic techniques can only be used in simplified geometries, i.e. axial symmetry. In principle, Monte Carlo techniques could be used to describe any situation -- the only limitation being computer speed and memory size. (It may take longer to calculate the situation than to build the shield and measure the result.)

The simple one-dimensional description of Lindenbaum²²⁾ provides a useful introduction. Suppose we have an incident high-energy primary particle which after a collision continues in the same direction at a reduced energy but with the same mean free path λ , or generates one or

more secondaries with the same λ until a sufficient number of collisions degrades the primary energy sufficiently (below 150 MeV -- where the absorption cross-section rises dramatically). Obviously, in reality there is a distribution function for the number of cascade collisions required to kill the primary and secondaries. For simplicity we suppose that a specific number n is required:



The number of particles that reach the plane X having made no collisions

$$= N_0 e^{-x/\lambda} . \quad (1)$$

Suppose there is one collision between O and X:

No. of particles that reach X =

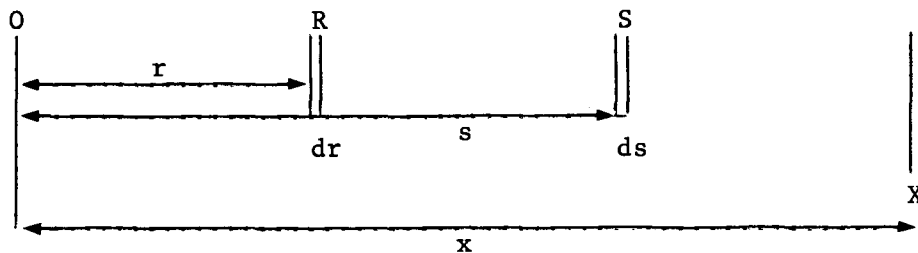
$$= \int_0^x N_0 e^{-r/\lambda} e^{-(x-r)/\lambda} \frac{dr}{\lambda} m_1$$

No. that reach dr
Probability of subsequently reaching X
Probability of interacting in dr

$$= \frac{N_0 m_1 x}{\lambda} e^{-x/\lambda} , \quad (2)$$

where m_1 is the multiplicity in the first interaction.

Suppose there are two collisions:



No. of particles that reach X =

$$\begin{aligned}
 &= \int_0^x \frac{N_0 m_1 s}{\lambda} e^{-r/\lambda} e^{-(x-s)/\lambda} \frac{ds}{\lambda} m_2 \\
 &\quad \begin{array}{ccc}
 \nearrow & \nearrow & \nwarrow \\
 \text{No. that reach S} & \text{Probability of} & \text{Probability of} \\
 \text{having made} & \text{subsequently} & \text{interacting} \\
 \text{one collision} & \text{reaching X} & \text{in ds}
 \end{array} \\
 &= \frac{N_0 m_1 m_2}{\lambda^2} e^{-x/\lambda} \int_0^x s ds = \frac{N_0 m_1 m_2 x^2}{2\lambda^2} e^{-x/\lambda} . \quad (3)
 \end{aligned}$$

We can therefore write, with n as defined above:

$$N_n(x) = N_0 \beta_n(x/\lambda) e^{-x/\lambda}, \quad \text{where } \beta \text{ is the build-up factor,}$$

$$\text{for } n = 1 \quad N_1 = (1)$$

$$\beta_1 = 1$$

$$\text{for } n = 2 \quad N_2 = (1) + (2)$$

$$\beta_2 = 1 + \frac{m_1 x}{\lambda}$$

$$\text{for } n = 3 \quad N_3 = (1) + (2) + (3)$$

$$\beta_3 = 1 + \frac{m_1 x}{\lambda} + \frac{m_1 m_2 x^2}{2\lambda^2} .$$

Therefore the build-up factor does not saturate but is a monotonically increasing function of x.

If $mx/\lambda \gg n$ ($m_1 = m_2 = \dots = m$), approximately exponential absorption takes place with a mean free path $= \lambda + \Delta\lambda$, where $\Delta\lambda = n\lambda/mx$. This correction becomes small as mx/λ increases, so to measure the true equilibrium mean free path we need thick shields.

(See Fig. 6 for an example with $m = 2$ where the exponential region is not achieved until $x/\lambda = 10$. For concrete this would mean a depth of $\sim 1200 \text{ g cm}^{-2}$.)

Analytical solutions of the one-dimensional transport equation for a real nucleon-meson cascade in slab geometry were given by Passow²³), Alsmiller²⁴), Barbier²⁵) and O'Brien²⁶). O'Brien used the transport equation in the form:

$$\left[\mu \frac{\partial}{\partial r} + \sigma_j(E) + \delta_{nj} \sigma_{Ej}(E) + \frac{\delta_{\pi^\pm j} + \delta_{K^\pm j}}{(P_j/m_j) c \tau_j} - (1 - \delta_{nj}) \frac{\partial}{\partial E} S_j(E) \right] \phi_{sj}(r, E, \mu) =$$

$$= \sum_{k=p, n, \pi^\pm, K^\pm} \int_{-1}^1 d\mu' \int_E^{E_{\max}} dE_B F_{jk}^t(E_B, E, \mu' \rightarrow \mu)$$

$$\times [\phi_{sj}(r, E_B, \mu') + \phi_{ij}(r, E_B, \mu')] , \quad (j, k = p, n, \pi^\pm, K^\pm)$$

where

- p, n, π^\pm, K^\pm = protons, neutrons, charged pions, and charged kaons, respectively,
- r = depth, in units of g/cm², in the slab,
- μ = cosine of the angle with respect to the normal of the slab,
- $\phi_{sj}(r, E, \mu)$ = flux per MeV of secondary particles of type j ($j = p, n, \pi^\pm, K^\pm$),
- $\phi_{ij}(r, E, \mu)$ = flux of primary particles of type j ,
- P_j = momentum of particle of type j in units of GeV/c,
- m_j = rest mass of particle of type j in units of GeV/c²,
- E = energy of flux in GeV,
- τ_j = mean life (in c.m.) of particle of type j ,
- c = velocity of light (in vacuo),
- $\sigma_j(E)$ = non-elastic cross-section for particles of type j , in cm²/g,
- $\sigma_{Ej}(E)$ = elastic scattering cross-section for neutrons, in units of cm²/g,
- $S_j(E)$ = stopping power of particles of type j in MeV cm²/g,
- $F_{jk}^t(E_B, E, \mu' \rightarrow \mu)$ = number of particles of type j per unit energy about E per unit solid angle travelling in a direction μ arising from a nuclear collision with a particle of type k ($k = p, n, \pi^\pm, K^\pm$) travelling in the direction μ' and having energy E_B .

$F_{jk}^t(E_B, E, \mu' \rightarrow \mu)$ has two components, and may be written

$$F_{jk}^t(E_B, E, \mu' \rightarrow \mu) = F_{jk}^{nel}(E_B, E, \mu' \rightarrow \mu)\sigma_j(E_B) + F_{jk}^{el}(E_B, E, \mu' \rightarrow \mu)\sigma_{Ej}(E_B) ,$$

where F_{jk}^{nel} and F_{jk}^{el} correspond to non-elastic and elastic processes.

Severe approximations and simplifications are necessary to find solutions for the fluxes, some of which are

- i) neglecting elastic scattering and ionization energy losses,
- ii) assuming constant absorption cross-sections,
- iii) assuming all secondary particle production to be in the forward direction and to be represented by a rather simple formula.

The results of the calculations agree well with relevant experimental data. Figure 7 gives the laterally integrated star density at $p_0 = 19.2$ GeV calculated by O'Brien and compared with experimental results²⁷⁾ and with a Monte Carlo calculation of Ranft. There is good mutual agreement.

O'Brien and McLaughlin²⁸⁾ describe an analytic cascade calculation in cylindrical geometry. They represent the neutron flux at depth r with energy E and direction cosine μ as a sum of four Legendre polynomials:

$$\phi_N(r, E, \mu) \sim \sum_{L=0}^{\xi} 1/2(2L + 1)F_L(r, E)P_L(\mu) ,$$

where

- r = depth in shield (g/cm^2);
- μ = the cosine with respect to the normal direction of the shield;
- $\phi_N(r, E, \mu)$ = the flux of neutrons per MeV at a depth r , having an energy E , and a direction cosine μ ;
- $P_L(\mu)$ = the Legendre polynomials of order L ;
- $F_L(r, E)$ = the Legendre coefficients of the flux.

It can therefore be used for shielding calculations for linear and circular accelerators. The upper energy limit of 500 MeV and the neglect of the meson and proton components could be said to restrict the

applicability to transverse shielding estimation, but owing to the finite transverse momenta of all produced secondaries, the energy range treated is sufficient to calculate the transverse development of the cascade for even the highest energy accelerators.

The results of these calculations were extensively compared with experimental values and Monte Carlo calculations, and it has been established that the results are in very good agreement. As an example, Fig. 8 compares the results of the calculations with experimental results.

The programs of O'Brien can also be made to predict neutron spectra in shielding. Figure 9 shows the result of such a calculation.

The Monte Carlo techniques are the most flexible for simulating problems of interest in radiation protection around proton accelerators. The most comprehensive is that of Armstrong, Alsmiller, Chandler and Bishop²⁹⁾; it is called HETC (high-energy transport code). It allows the source particles (p, n, π^\pm , μ^\pm) to be arbitrarily distributed in angle energy and space, and its geometry routines are very flexible. In the initial analysis a complete history of each event is written on to a magnetic tape which can then be analysed at will for the items of interest. It follows events down to about 15 MeV and can give details of the isotopes left after the nuclear interactions. However, it takes typically three hours of CPU time on an IBM 360/75 to write the basic tape, and it is not a "general use" engineering program.

The CASIM program written by Van Ginneken at FNAL³⁰⁾, apart from the variance reduction techniques is based on the programs of Ranft³¹⁾, which have been in existence since 1965. Ranft's Monte Carlo programs do not treat the intranuclear cascade and evaporation stages as separate entities. Since the intranuclear cascade contains essentially particles below 1 GeV, it does not significantly affect the growth of the extranuclear hadron cascade; and so in the deep penetration code TRANKA¹³⁾, the small dump code FLUKA¹³⁾, and the target + cylindrical shield code MAGKA³²⁾, particle production is based only on the multiple-production formulae of Section 3.1. It is, however, taken into account with a modified production formula³³⁾ in the modified cylindrical shield code MAGKO³⁴⁾ and the target production code FLUKU³³⁾. All these programs are designed for the CDC 7600 and take from 60 to 1000 sec to obtain meaningful results.

Output is in the form of graphs of energy density (GeV/cm^3) or star density (stars/cm^3) as a function of position (FLUKU and TRANKA give particle flux densities in addition).

From the design point of view, energy density is related to radiation heating in targets, septa, etc., and to absorbed dose which is linked to radiation damage to components; star density is related to hadron flux density and to remanent radioactivity. All of these are of vital interest in considering the radiation environment of the machine.

We can answer the questions as to how accurate are these codes and what they can do in explaining the radiation environment by looking at comparisons between experimental data and the predictions of the programs. This will be one of the guidelines of the following sections.

5. THE PROMPT FIELD CLOSE TO THE ACCELERATOR

This may seem somewhat academic to the accelerator health physicist, but there is a golden rule for proton accelerators (not so true for electron accelerators):

if a component dies because of radiation damage, someone will receive a significant dose during its replacement and/or repair:

$$\begin{array}{lll} 20 \text{ Mrad/year} & \equiv & 1 \text{ rem/hour} \\ \text{prompt dose-rate} & & \text{remanent dose-rate} . \end{array}$$

In addition, should someone be accidentally left inside a shielded enclosure, it would be useful to have some knowledge of the radiation environment.

Extensive yield data for low-energy particle flux and dose around targets bombarded by 7 and 24 GeV protons are given in Stevenson et al.³⁵⁾. Routti³⁶⁾ gives results at 22 GeV/c using spallation detectors. The comparison of the program MAGKO with some of these data are given in Figs. 10-12. A full comparison will be given by Ranft and Stevenson³⁷⁾. From these comparisons it will be seen that the Monte Carlo calculations agree well with the data and contain no more scatter than the experimental points do.

Useful extrapolations to new situations can always be made from the experimental data, but when the cascade is partially developed the Monte

Carlo calculations offer the only way of estimating particle flux densities or dose apart from a direct simulation experiment (compare 100 sec of CDC 7600 CPU time with days of experiment).

Close to beam interaction points the electromagnetic cascade generated from the decay of π^0 mesons assumes some importance, especially for heavy target materials and/or high incident proton energies, as will be seen from Table 6³¹⁾.

Table 6

Percentages of the incident proton energy deposited
in the cascade by the various mechanisms

p_0 (GeV/c)	8	20	50	100	300
Ionization	24	22	19.5	17	15.5
π^0 mesons	27	36	43.5	50.5	56
Excitation	45	39	34.5	30	26.5
Particles with $E < E_{thr}$	4	3	2.5	2.5	2

Thus, even at 20 GeV, 60% of energy deposition (dose) comes from minimum ionizing particles; this rises to 70% at 300 GeV.

Energy deposition has significant effects on target design, in so far as temperature rise is concerned (see Table 7). For this reason, all targets at the CERN Super Proton Synchrotron (SPS) will be made of Be or Al. FNAL use heavier targets at reduced proton intensities. A badly canned uranium target was disrupted by the Nimrod 7 GeV proton beam causing significant contamination of an extracted beam blockhouse. Decontaminating such an area is a health physics task which is preferably avoided.

Table 7

Radiation heating (short burst)
300 GeV/c, 10^{13} incident protons³⁸⁾

	ΔT ($^{\circ}C$)
Cu target 2×2 mm ²	1000
Al target 2×2 mm ²	350
W target 2×2 mm ²	3700
Fe beam dump, beam 2 mm ϕ maximum	1000

6. THE SHIELDED HADRON COMPONENT

Our knowledge of the hadron component of the radiation environment outside the shielding of high-energy proton accelerators is limited by the available detection techniques which have sufficient sensitivity. A summary is given in Table 8. It will be seen that very few of the detectors are specific to one type of particle or to one energy region. However, when used together they allow us to describe the radiation environment in broad terms.

Table 8

Particle detection techniques

Detector	Technique	Contributing particles
Kodak RM film	Photometry	All charged particles
Nuclear track emulsions	Track density "Enders" Star density (prong-counts of stars gives an idea of spectral index) Proton recoils	Minimum ionizing particles Hadrons > 50 MeV Hadrons > 50 MeV Neutrons 0.5-20 MeV
BF ₃ tube or ⁶ LiI crystals	α-particle counting	Thermal neutrons
As above + hydrogenous moderator	α-particle counting	Neutrons, thermal-20 MeV Hadrons > 50 MeV
Sulfur activation	³² P assay	Neutrons > 3 MeV
Aluminium activation	²⁴ Na assay ¹⁸ F or ²² Na assay	Neutrons > 6 MeV Hadrons > 50 MeV
Plastics activation	¹¹ C assay	Hadrons and photons > 20 MeV
Bismuth fission	Ionization chamber	Hadrons > 50 MeV
Spark chamber, telescopes	Proton recoil spectrometry	Protons and muons > 20 MeV and/or neutrons > 20 MeV
⁷ LiF	Thermoluminescence	All charged particles
⁶ LiF	Thermoluminescence	All charged + thermal neutrons
Air/argon ionization chambers	Charge or current measurement	All charged particles
Hydrogen ionization chambers	Charge or current measurement	All charged + neutrons > 0.3 MeV

From emulsion experiments we get some idea of the star and track density as a function of position in the shield (see Figs. 13-16)³¹⁾. But for a complete description of the radiation environment where the different detectors need to be used together and also need to be calibrated as a set, the published data available are very scarce indeed. Some are given in Table 9.

On the assumption that all the detector response comes from neutrons, the techniques are available to unfold neutron energy spectra⁴²⁾, but the validity of the spectra is entirely dependent on the input data. For example, the presence of protons or photons would entirely distort the interpretation for the $^{12}\text{C} \rightarrow ^{11}\text{C}$ data where the proton cross-section is at some energies four times the neutron cross-section. However, for what they are worth, Fig. 17 shows some typical spectra⁴³⁾. That the spectra are not entirely fictitious is illustrated by the relative agreement between the cosmic-ray spectra of Hess et al.⁴⁴⁾ and the calculations of Armstrong et al.⁴⁵⁾ [see Fig. 18 which is taken from Rindi and Thomas⁴⁶⁾].

However much disagreement there is in the details of spectra, there is general agreement that a maximum of three detectors are needed to determine dose equivalent. If we do not talk about LET spectrometry or recombination chambers, we need a moderated thermal neutron detector, a detector based on $^{12}\text{C} \rightarrow ^{11}\text{C}$, and an air ionization chamber, or similar. There is less agreement on the exact numbers which should be used to convert the flux densities to dose equivalent (DE). What is agreed is that to obtain consistency between the Andersson Braun Moderator assembly for "Rem counters or Rem ion chambers" and other moderators, a number like $15 \text{ ncm}^{-2} \text{ sec}^{-1}/\text{mrem h}^{-1}$ has to be used for 5-inch \emptyset moderators and $7 \text{ ncm}^{-2} \text{ sec}^{-1}/\text{mrem h}^{-1}$ for 10-inch \emptyset moderators. However, in most accelerator spectra the Andersson Braun is expected to overestimate the dose equivalent from neutrons below 20 MeV by up to a factor of 2. For the ^{11}C technique, on the assumption that all the response is due to neutrons, the conversion number would be $3 \text{ ncm}^{-2} \text{ sec}^{-1}/\text{mrem h}^{-1}$, giving the DE from neutrons with energies $> 20 \text{ MeV}$. *But* with the presence of a proton component in the ratio $\sim 0.8 \text{ p/n}$ in the relevant energy region [Wright⁴⁷⁾ -- calculated for tissue but assumed for concrete; Ranft also gives a ratio of $n:p:\pi^{\pm}$ of 2:1:1 for cascades in iron] and assuming that the directly ionizing part of the proton dose is picked up by the ion chambers, the relevant conversion number is $10 \text{ "n" cm}^{-2} \text{ sec}^{-1}/\text{mrem h}^{-1}$ to give the high-energy non-directly ionizing, inelastic interaction part of the dose equivalent.

Table 9

Experimental response data

Position and shield	Reference	Bismuth fission chamber (220 MeV n) cm ⁻² sec ⁻¹	¹² C + ¹¹ C (22 mb) cm ⁻² sec ⁻¹	²⁷ Al + ²⁴ Na (120 mb) cm ⁻² sec ⁻¹	Moderated BF ₃ or In,Au (Pu-Be n) cm ⁻² sec ⁻¹	Bare In,Au therm. cm ⁻² sec ⁻¹	Air ionization chamber or TLD mrad/h	rem-ion chamber mrem/h
CERN ring top concrete + earth	39	35	62	19	40	-	2.3	-
CERN shield bridge iron + concrete	39 (normaliz.)	1.2	2.3	0.79	4.3	-	-	-
Bevatron unspecified shield	39 (normaliz.)	0.96	1.8	0.73	6.2	-	-	-
CERN PS end-stop iron + concrete	40	-	9340	3150	49.500	6920	-	-
Nimrod target side shield iron + concrete	41	-	600	155	450	220	20	95

7. THE DIRECT MUON COMPONENT

Behind the end-stop of most secondary pion or kaon beams or behind proton end-stops when the proton energy is greater than ~ 20 GeV, muons will give rise to a significant fraction of the total dose equivalent. At lower proton energies the shielding required for hadron attenuation is usually sufficient to eliminate the muons. Since muons are weakly interacting particles they can only be stopped by "ranging them out". Table 10 gives muon ranges (rounded) when all loss mechanisms are considered^{48,49}.

Table 10

Muon range as a function of momentum

Momentum (GeV/c)	Range (m)		
	Iron $\rho = 7.8$	Earth $\rho = 2.0$	Lead $\rho = 11.3$
1	0.7	2.4	0.65
2	1.5	5	1.3
5	4	15	3
10	7	25	6
20	15	45	10
50	30	110	25
100	55	205	40
150	80	290	50
200	100	380	60
300	130	530	80
400	160	670	100

Muons lose their energy by four processes: ionization, pair production, bremsstrahlung, and nuclear interactions. These are discussed in detail by Richard-Serre⁵⁰).

i) Ionization and excitation

The density-corrected Bethe-Block formula is used:

$$\frac{dE}{dx} = -2m_e c^2 \pi r_e^2 N \frac{A}{Z} \frac{1}{\beta^2} \left(\ln \frac{(2m_e c^2 \eta^2)^2}{I^2 \left[1 + \frac{m_e}{M} \sqrt{1 + \eta^2} + \left(\frac{m_e}{M} \right)^2 \right]} - 2\beta^2 - \delta - 2 \frac{c_e}{Z} \right).$$

m_e, r_e mass and classical radius of electron
 Z, A, I atomic number, weight, and ionization potential of material
 δ, c_e density effect and screening corrections
 M muon mass
 $\eta = \beta\gamma; \beta = v/c; \gamma = 1/(1 - \beta^2)^{1/2}$.

ii) Electron pair production

$$\frac{dE}{dx} = - \frac{N}{A} \frac{m_e}{M} \frac{(\alpha Z r_e)^2}{\pi} E \left[19.3 \ln \left(\frac{E}{Mc^2} \right) - 53.7 \right] \times f ,$$

where f is a screening factor which is 1 up to a muon energy of $28 - 0.36Z + 0.002Z^2$ (GeV). Above this energy

$$f = \left[\frac{16}{9} \ln (183Z^{-1/3}) + 1 \right] \left[\frac{16}{9} \ln \left(\frac{E}{Mc^2} \right) - \frac{14}{9} + \ln 2 \right]^{-1} .$$

iii) Bremsstrahlung

$$\frac{dE}{dx} = -4\alpha N r_e^2 \frac{Z^2}{A} \left(\frac{m_e}{M} \right)^2 E \left[\ln \left(\frac{12E Z^{-1/3}}{5Mc^2} \right) - \frac{1}{3} \right] .$$

iv) Nuclear interactions

$$\frac{dE}{dx} = - \frac{2N}{\pi} \alpha \sigma_\gamma E ,$$

where σ_γ is the effective photonuclear cross-section of the muon (energy independent and equal to 120 μb).

Numerically, bremsstrahlung losses are approximately equal to pair production losses; they become significant in the 50 GeV region.

All energy loss processes are stochastic, with the result that for a muon of a given energy there is no unique range. These effects have been calculated in detail by Atherton⁵¹). Table 11 summarizes his main results.

Thus the use of the mean range from ionization losses alone as an upper limit to the range of the muon only becomes really effective at energies greater than 400 GeV.

Table 11

Effect of straggling on muon ranges

Shield	Momentum (GeV/c)	Most muons stop at (m)	10% e x c e e d (m)	1% (m)	0.1% (m)	Full loss range (m)	Ionization only (m)
Iron $\rho = 7.2$	200	110	120	132	140	105	132
	400	190	205	220	228	175	260
	50	110	120	130	135	105	110
Earth $\rho = 2.0$	100	210	220	235	245	205	210
	200	390	410	430	445	380	410
	400	710	740	780	800	670	815
	500	870	890	930	950	800	1010

For biological shielding we rarely aim to range out the muon completely but to dilute the muons by multiple scattering etc. to a sufficiently low level. Since we are not working near the end-point of the muon's range, we can afford to neglect straggling in our calculations except when very high attenuation is required. The cost of a muon shield varies only linearly with its length, but varies as the square of its lateral dimension, i.e. changing from a radius of 2.5 m to 3 m adds 50% to its cost. Thus it is imperative to understand the physical processes that broaden a once-parallel beam of muons and to know the initial angular and momentum distribution of the muons as they are created.

Let us now run quickly through the various physical processes involved in muon production and transport.

7.1 Probability of decay

All charged pion decays and 65% of charged kaon decays result in a single muon (+ neutrino). We can neglect the other modes of production.

p = parent momentum in GeV/c.

ϵ_0 = rest mass energy of parent in GeV.

$p = \gamma\beta\epsilon_0$ [$\gamma = 1/(1 - \beta^2)^{1/2}$; $\beta\gamma = v/c$].

Mean lifetime in laboratory frame $\tau = \gamma\tau_0$ (τ_0 = rest frame lifetime).

Convert to decay length: $\lambda = v\tau = \beta\gamma\tau_0 c$

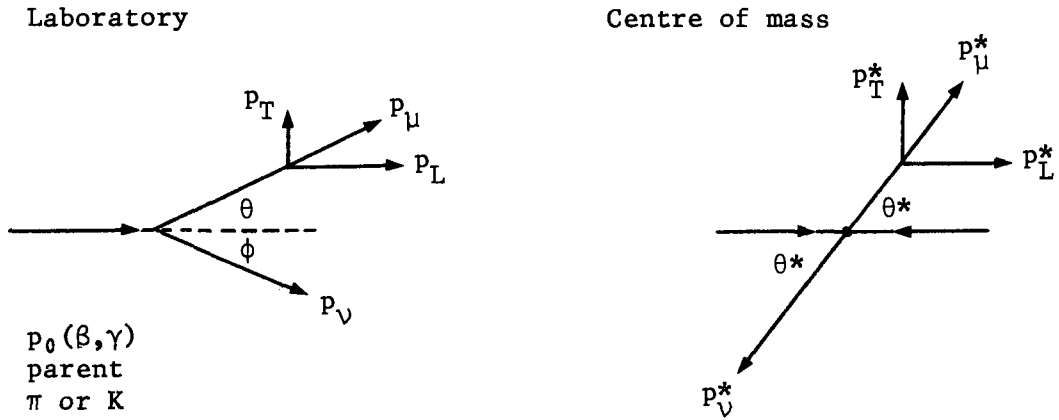
$= p \times \tau_0 c / \epsilon_0$.

For pions $\lambda = p \times 2.55 \times 10^{-8} \times 2.998 \times 10^8 / 0.1396$
 $= 54.76 \text{ m per GeV/c};$

for kaons $\lambda = p \times 1.229 \times 10^{-8} \times 2.998 \times 10^8 / 0.4938$
 $= 7.46 \text{ m per GeV/c};$

e.g. number of muons produced by a beam of 10^7 pions per burst at
 10 GeV/c in a length of 50 m $= 10^7 \times 50 / (55 \times 10) \sim 10^6$ muons per burst.

7.2 Decay kinematics



In the centre of mass:

$$p_{\mu}^* = p_{\nu}^* \quad \text{and} \quad E_{\mu}^* + E_{\nu}^* = E_0 ,$$

hence

$$p_{\mu}^* = (\epsilon_0^2 - \epsilon_{\mu}^2) / 2\epsilon_0$$

and

$$E_{\mu}^* = \sqrt{\epsilon_{\mu}^2 + p_{\mu}^{*2}} = (\epsilon_0^2 + \epsilon_{\mu}^2) / 2\epsilon_0 .$$

Parent	p_{μ}^*	E_{μ}^*
π (139.58 MeV)	29.81 MeV/c	109.774 MeV
K (493.8 MeV)	235.60 MeV/c	258.20 MeV
μ (105.65 MeV) .		

In the laboratory frame:

$$p_L = \gamma(p_{\mu}^* + \beta E_{\mu}^*) = \gamma(p_{\mu}^* \cos \theta^* + \beta E_{\mu}^*)$$

$$p_T = p_T^* = p_{\mu}^* \sin \theta^*$$

$$\tan \theta = p_T / p_L .$$

Minimum energy occurs when $\theta^* = 180^\circ$ (assume $\beta = 1$):

$$\begin{aligned} p_{\min} &= p_L = \gamma(-p_\mu^* + E_\mu^*) = p_0(E_\mu^* - p_\mu^*)/\epsilon_0 \\ &= p_0(\epsilon_\mu^2/\epsilon_0^2) \\ &= 0.57 p_0 \text{ for pion parents, or} \\ &= 0.046 p_0 \text{ for kaon parents .} \end{aligned}$$

The maximum angle of emission in the lab. occurs when $\cos \theta^* = -(p_\mu^*/E_\mu^*)$,
i.e.

$$\tan \theta_{\max} = \frac{1}{p_0} \frac{\epsilon_0 p_\mu^*}{\epsilon_0} .$$

Table of θ_{\max} in milliradians:

Momentum Parent	5	10	20	50	100	200	400
π	7.8	3.9	2.0	0.79	0.39	0.20	0.10
K	217	110	55	22	11	5.5	2.8

i.e. one can assume that π - μ decays are essentially collinear, but the decay angles of the K- μ decay mean that the muon cone has a significantly wider divergence than its kaon parent beam.

7.3 Momentum distribution

In the centre-of-mass system the decay is isotropic

$$\therefore \frac{dN}{d\theta^*} = \frac{1}{2} \sin \theta^* .$$

In the lab. system

$$\frac{dN}{dp_\mu} = \frac{dN}{d\theta^*} \cdot \frac{d\theta^*}{dp_\mu} .$$

$$\text{Now } p_\mu^2 = \gamma^2(p_\mu^* \cos \theta^* + \beta E_\mu^*)^2 + (p_\mu^* \sin \theta^*)^2 .$$

Let $p_{\min}/p_0 = k = \epsilon_\mu^2/\epsilon_0^2$ and put $\beta = 1$:

$$\therefore p_\mu^2 = \frac{p_0^2}{4} [(1 - k) \cos \theta^* + 1 + k]^2 + \frac{\epsilon_0}{4} (1 - k)^2 \sin^2 \theta^* .$$

Assume $p \gg \epsilon_0$:

$$\therefore p_\mu = \frac{p_0}{2} [(1 - k) \cos \theta^* + 1 + k]$$

$$\therefore \frac{dp_\mu}{d\theta^*} = \frac{p_0(1 - k) \sin \theta^*}{2}$$

$$\therefore \frac{dN}{dp_\mu} = \frac{1}{p_0(1 - k)},$$

i.e. is independent of momentum p_μ and extends uniformly from the parent momentum p_0 to the minimum momentum p_{\min} .

7.4 Cascade muons

So far, the only direct calculations of muons produced in a hadron cascade have been those of Ranft⁵²⁾ *). However, following the work of Keefe⁵³⁾ using the analytic cascade calculations of Riddell⁵⁴⁾, most people assume that the muon distribution is simulated by allowing pions and kaons from the *first* proton interaction to have a decay length of $1.8 \times$ the interaction muon free path for protons in the material.

7.5 Muon scattering

The Eyges solution of the Boltzmann diffusion equation for the spatial and angular distribution of muons, originally having a single momentum vector p_0 , gives

$$\psi(p_0, z, r) = \frac{1}{4\pi A_2(p_0, z)} \exp \left[- \frac{r^2}{4\pi A_2(p_0, z)} \right]$$

as the flux of muons at a position (r, z) in the shield, integrated over all angles, where

$$A_2(p_0, z) = \int_0^z \chi^2 [p(p_0, z'), z'] (z - z')^2 dz' ;$$

χ^2 is one-quarter of the mean square scattering angle per unit distance; the integral sums up the displacements at z due to scattering in dz' at z' [see Alsmiller et al.⁵⁵⁾].

Contributions to χ^2 come from all the effects already mentioned, i.e. multiple Coulomb scattering, pair production, bremsstrahlung, and nuclear interactions. Their relative importance is illustrated in Fig. 19, and

*) Note added in proof: Calculations of both prompt and cascade muons are included in the recent work of Van Ginneken⁷⁶⁾.

the effect of ignoring scattering other than Coulomb is illustrated in Fig. 20⁵⁵⁾. At momenta up to 100 GeV/c one can ignore the non-Coulomb scattering, but above this energy, non-Coulomb effects assume an increasing importance.

Each effect is assumed to give rise to a Gaussian distribution which is certainly not true of Coulomb scattering beyond 3σ from the mean where the so-called Molière scattering occurs. However, at energies less than 100 GeV one simplifies the problem by assuming only Gaussian Coulomb scattering of the form

$$4\chi_C^2 = \left(\frac{0.021}{p} \right)^2 \frac{1}{X_0},$$

where p is in GeV/c and X_0 is the radiation length. We can then write

$$A_2 = \frac{1}{4} \int_0^z \frac{0.021^2}{X_0} \frac{(z - z')^2}{p(z')^2} dz'.$$

Keefe and Noble⁵³⁾ put $p(z') = p_z + b(z - z')$ and $z - z' = y$. Thus

$$\begin{aligned} A_2 &= \frac{1}{4} \frac{0.021^2}{X_0} \int_0^z \frac{y^2 dy}{(p_z + by)^2} \\ &= \frac{1}{4} \frac{0.021^2}{X_0} \frac{1}{b^3} p_0 \left[1 - \left(\frac{p_z}{p_0} \right)^2 + \left(\frac{p_z}{p_0} \right) \log \frac{p_z}{p_0} \right]. \end{aligned}$$

This form gives adequate accuracy provided a suitable effective value of b is chosen, namely the average over the distance z through matter in which the momentum is reduced from p_0 to p_z .

8. RADIATION ESCAPING FROM TUNNELS AND DUCTS

Every accelerator has holes in its shielding for the access of personnel to the accelerator areas or for the passage of cables and ventilation ducts. The change in spectrum of the radiation with distance along the duct differs somewhat from the change in spectrum with distance through a thick shield. In the first leg of a tunnel (measured from the inside of the shield) where the tunnel has full view of a point source, the transmission is essentially inverse square, modified by an absorption cross-section which depends on energy and radiation type [see Figs. 21 and 22³⁹⁾ and Table 12].

Table 12

Attenuation lengths and removal cross-sections
for tunnel transmission

Detection technique	Attenuation length (metres)	Removal cross-section (barns)
$^{12}\text{C} \rightarrow ^{11}\text{C}$	100	1.9
$^{27}\text{Al} \rightarrow ^{26}\text{Na}$	60	3.2
Film badge and TLD	55	3.3
$^{197}\text{Au} \rightarrow ^{196}\text{Au}$	30	6.2

After a right-angled bend, all components suffer a more rapid attenuation than for the corresponding distance along a straight tunnel. The effect is more marked the higher the neutron energy [see Fig. 23 ⁵⁶]. In multilegged ducts one can deduce the attenuation of the tunnel purely by considering neutrons below 10 MeV. For the first leg where the source is off-axis, and for the second and subsequent legs of a duct, the attenuation is essentially a function of the depth in the leg divided by the square root of the cross-sectional area. "Universal attenuation curves", which are a mixture of many calculations and experiments, are given in Figs. 24 and 25 ⁵⁷).

9. SKYSHINE (AIR-SCATTERED RADIATION)

Since this is to be treated in detail in another lecture during the course, it will be sufficient to say here that when a direct view of the shield of a major loss point is possible, the environment will be characteristic of the developed cascade in air after a suitable transition distance -- this should not be very different, apart from density effects, from the developed cascade in concrete. However, if the direct view is shielded by ground or buildings, one will only be able to see the wide-angle particles produced in the cascade-air nucleus interactions. Thus low-energy (< 10 MeV) neutrons should predominate [see Rindi and Thomas ⁵⁸].

In a preliminary estimate of air-scattered radiation it is sufficient to assume, for the indirect view, that every ^{11}C particle that leaves the shield is transformed into a lower-energy neutron⁵⁹⁾, i.e. the dose-equivalent rate at a distance r is given by

$$H(r) = \frac{\phi \cdot A}{2\pi r^2} \text{ g rem/h} ,$$

where ϕ is the flux density of ^{11}C particles ($\sigma = 22 \text{ mb}$) leaving a shield of area A , and g is the dose-equivalent rate per unit flux density for lower-energy neutrons ($\sim 15 \text{ n cm}^{-2} \text{ sec}^{-1} \equiv 1 \text{ mrem/h}$).

10. INDUCED RADIOACTIVITY -- ACCELERATOR STRUCTURE

In the reaction of a high-energy hadron with a nucleus, a hadron cascade is developed within the nucleus. After the emission of particles from this cascade, further particle emission occurs by nuclear evaporation from the excited nucleus. This type of interaction is termed spallation. Lower-energy neutrons interact with nuclei via resonance processes, but these generally result in the removal of only a few nucleons from the struck nucleus. The daughter nucleus from either type of interaction is not necessarily radioactive. Furthermore, not all of the radioactive daughter nuclei contribute directly to the dose-rate measured several hours after the irradiation: those isotopes having very short half-lives will have decayed already, while those with long half-lives will not decay at a rate high enough for them to contribute significantly to the dose-rate. The remanent dose-rate does not therefore depend on the Z and A of the struck nucleus in a simple way; each nucleus must be considered individually, especially in relation to the number of radioactive nuclei below it in the Periodic Table whose half-lives are between several hours and several months, and in relation to the number and energies of the gamma-rays emitted from these isotopes.

There are extensive experimental data on the cross-sections for the production of a particular radioisotope from a given target nucleus by proton interactions [see, for example, Bruninx⁶⁰⁾]. An empirical relationship describing these data was derived by Rudstam⁶¹⁾: this can be used to derive cross-sections for isotopes and at energies for which no experimental data are available. It is also possible to predict these

cross-sections from the intranuclear cascade calculations of Bertini¹⁶). This is the necessary input information for calculations of dose-rate due to direct mono-energetic proton interactions in targets and septum elements: these calculations are described in some detail by Barbier⁶²). The cross-section information can be combined with models of the development of the extranuclear hadron cascade in order to predict the spatial distribution of radioisotopes in extended targets such as magnet units. Calculations of this type for large iron targets have been performed by Armstrong⁶³), and have shown good agreement with the available experimental data. Armstrong and Alsmiller⁶⁴) combined these calculations with photon transport calculations in order to predict the gamma dose-rate from the radioisotopes produced by interactions in a simulated magnet unit for the American 200 GeV accelerator. Their calculated variation of dose-rate with irradiation time and cooling time is shown in Fig. 26⁶⁵); a typical decay curve for a magnet unit in the CERN PS is also shown in this figure, as is the empirical formula for decay derived by Sullivan and Overton⁶⁶).

They showed that the decay of dose-rate from an iron-dominated environment could be represented by an equation of the form

$$D(t) = k \log [(t_i + t)/t] ,$$

where $D(t)$ is the dose-rate at a time after the irradiation has stopped, and t_i is the irradiation time.

The Oak Ridge calculations⁶⁷) (see Fig. 27) indicate the dominant isotopes: ^{54}Mn (280 d), ^{52}Mn (5.6 d), ^{48}V (16 d), ^{51}Cr (27.8 d), ^{56}Mn (2.6 h), ^{52}Mn (21 min), ^{56}Co (77.3 d), ^{51}Mn (46.5 min), ^{44}Sc (4 h), and ^{49}Cr (42 min).

One can estimate the remanent dose-rates from hadron star densities in iron in a number of ways. The simplest is to realize that $\sim 10\%$ of all inelastic interactions give rise to a gamma-emitting isotope whose half-life is such that it could contribute to the dose-rate after a day's cooling. The saturation activity for these isotopes for a star production rate of 1 star/(cm³ sec) is

$$\frac{0.1}{3.7 \times 10^4 \times 7.8} \mu\text{Ci/g} = 3.5 \times 10^{-7} \mu\text{Ci/g} .$$

The standard health physics formula for the dose-rate from a semi-infinite slab is

$$D = 1.07 \times c(\mu\text{Ci/g}) \times E(\gamma \text{ energy in MeV})\text{rem/h} .$$

The average energy of gammas from iron is ~ 1 MeV. Therefore the dose-rate for 1 day cooling, infinite irradiation, is $\sim 4 \times 10^{-7}$ (rem h⁻¹)/(star cm⁻³ sec⁻¹). So from Fig. 26 for a 30 days irradiation (our standard at CERN) we would have

$$\omega_{30,1} \sim 1.5 \times 10^{-7} \text{ (rem h}^{-1}\text{)/(star cm}^{-3} \text{ sec}^{-1}\text{)} .$$

But this refers to the actual density of stars, which is larger by a factor of 3-5 than star densities calculated by Ranft programs⁶⁸). So in reality

$$\omega_{30,1} \sim 5 \times 10^{-7} \text{ (rem h}^{-1}\text{)/(star cm}^{-3} \text{ sec}^{-1}\text{)} .$$

Another way is to directly superpose the calculations of Oak Ridge and Ranft made for the same geometry⁶⁹) (Figs. 28 and 29). The conversion factor then comes to $\sim 1.5 \times 10^{-6}$ (rem h⁻¹)/(star cm⁻³ sec⁻¹). We have suspected for some time that these Oak Ridge calculations of remanent dose-rate are somewhat conservative. Recent experiments by Hofert et al.⁷⁰) have confirmed that for steel a better value is $\sim 5 \times 10^{-7}$ (rem h⁻¹)/(star cm⁻³ sec⁻¹).

11. ACTIVATION OF ELEMENTS OTHER THAN IRON

This subject is dealt with in a very comprehensive way by Barbier⁶²), and here we will summarize only his main conclusions. In a given irradiation situation where the remanent activity is predominantly due to spallation reactions, there is a tendency for the dose-rate to increase with atomic number up to elements in the molybdenum region. This effect is illustrated in Fig. 30⁶⁵). Above this region the dose-rate decreases slightly as the atomic number increases, but Barbier does point out the limitations of the Rudstam formula in this high-Z region. The low specific dose-rate for elements in the calcium region is due to lack of gamma-emitting isotopes with sufficiently long half-lives in this region of the Periodic Table: here the gammas emitted from the isotopes

of sodium predominate. For irradiated plastics and oils the isotopes which will contribute to the remanent dose-rate are ^7Be (53.6 d) and ^{11}C (20 min).

12. ACTIVATION OF CONCRETE

Unlike cast-iron and steel, which are relatively pure substances, concrete is a heterogeneous mixture of a variety of compounds. An average atomic composition for a typical concrete aggregate is difficult to specify: the composition will vary with the geographical location from which the aggregate was taken.

Because of this variation in composition, in the subsequent discussion we shall standardize on a concrete aggregate that contains 1% by weight of sodium and whose elemental composition is otherwise like that of a normal concrete.

There have been a number of experimental investigations into the activation of concrete by the developed hadron cascade, but the only theoretical estimates of remanent dose-rate in this situation are those of Armstrong and Barish⁷¹⁾ for the Batavia accelerator. All estimates and measurements agree that for a cool-down time of ~ 10 min, the remanent dose-rate from the ^{24}Na induced in the concrete is ~ 20 times the dose-rate from all other radioisotopes. (The other isotopes which can contribute are ^7Be , ^{11}C , ^{13}N , ^{22}Na , ^{34}Cl , and ^{38}K .) After one hour cool-down time this ratio is nearer 100. Thus for dose-rate predictions, in this situation it is only necessary to consider the production mechanisms for ^{24}Na .

Sodium-24 can be formed from spallation reactions of higher-Z nuclei in the aggregate or from the (n,γ) reaction by thermal neutrons on ^{23}Na . This latter reaction is by far the most important production mechanism. For example, Armstrong and Barish⁷¹⁾ predict that 25 times as much ^{24}Na activity is produced from ^{23}Na as from all spallation reactions together; Gilbert et al.⁷²⁾ show that between 2 and 10 times as much ^{24}Na activity is produced by thermal neutrons as by all other particle types. Thus when estimating the dose-rates to be expected from active concrete, it is safe to take as the hadron spectrum incident on the wall, that spectrum which contains the maximum number of thermal neutrons. In the geometry

considered by Armstrong and Barish, that of a uniform number of interactions per unit length along the axis of an iron cylinder, the largest proportion of thermal neutrons could be expected to occur for a cylinder radius of between 100 and 200 g/cm², i.e. the radius chosen to represent the FNAL magnets (160 g/cm²) should provide these "worst estimates". For a tunnel radius of 2 m, the dose-rate after a lapse-time of 6 min is 1.5×10^{-9} (rem h⁻¹)/(primary interactions cm⁻¹ sec⁻¹) for a primary energy of 3 GeV: this figure can be expected to scale as proton energy and to decay with the 15-hour half-life of ²⁴Na.

But even after 6 min cool-down time, the dose-rate from remanent activity in the wall and measured at the wall face, is only three times greater than the dose-rate from remanent activity in the iron, also measured at the wall face; at positions closer to the magnets this ratio will be smaller. Thus after the standard 24 hours cool-down time, the dose-rate from concrete activity will always be smaller than or about equal to the dose-rate activity in the iron, and is therefore not expected to dominate the dose-rate situation when one is trying to consider problems of access to any specified area around an accelerator. If, however, access after a short cool-down time is required, then the dose-rate from the concrete may be the critical parameter; then it is possible to reduce this dose-rate in a variety of ways. Table 13 ⁶⁵⁾ shows that reductions by at least a factor of 3 in this dose-rate from remanent activity in the concrete can be provided.

Table 13

Methods of reducing dose-rates from activity induced in concrete

Method	Reduction factor	Ref.
0.8% B addition by weight	10	72
0.3% B addition by weight	3	73
0.1% B addition by weight	9	71
0.166 g/cm ² B coating	3	
1/32" Cd coating	2.7	

13. INDUCED ACTIVITY -- AIR AND WATER

Radioactive nuclei are produced by spallation and other reactions in the air and water which are necessary for cooling accelerator components. Forced air convection to remove heat from targets or septum elements can lead to levels of radioactivity which would give rise to significant problems at the fence post if the air were to be vented quickly⁷⁴). Only the following radionuclides need to be considered: ^3H , ^7Be , ^{13}N , ^{11}C , ^{15}O , and ^{41}A . For all of these isotopes the maximum permissible concentration in air is governed by the external dose-rate hazard. Thus a measurement of induced radioactivity with a thin-walled ionization chamber will automatically include the hazard from radioactive gases in its assessment.

Radioactivity induced in cooling water is dominated by ^3H , ^7Be , ^{11}C , ^{13}N , and ^{15}O , and some radioactive corrosion products. Beryllium-7 is effectively removed in ion exchange resins, causing some experimental problems in their regeneration; ^3H will be vented to the air in the heat exchangers: the other activation products can give rise to significant dose-rates close to the pipes carrying the water. If these pipes stay in the accelerator enclosures this should not cause problems; however a significant nuisance can arise if these pipes pass through an otherwise quiet zone.

The environmental impact of the radioactivity produced in air and water is too large a subject to be treated here.

14. PROTON SYNCHROTRONS VERSUS STORAGE RINGS

Since the radiation environment of both types of machines depends on proton interactions with targets, dumps, or the accelerator structure, the physical nature of the environment in the two cases must be identical. [For a complete description of problems arising from ISR operation, see Tuyn⁷⁵].

In a conventional PS, shielding of the ring has to be designed for beam losses during injection, transition, internal targetting, ejection, scraping, and internal dumping. In an ISR the object is *not* to lose beam at all. Thus the shielding has to be designed for scraping on injection, clean-up scraping, and dumping (plus maybe catastrophic unintentional dumping). Proton-proton and proton-"vacuum" interactions are negligible.

Thus the only difference in the prompt radiation environment is in its time structure -- losses occur each cycle on a PS but only at irregular, well-spaced intervals on an ISR.

As far as induced radioactivity is concerned, apart from dumps and scrapers, an ISR is a clean machine with remanent dose-rates rarely exceeding a few mrem/hour. At FNAL and the CERN SPS it is difficult to keep remanent dose-rates close to ejection components, for example, to less than a few rem/hour; and in an ISR one never has the induced activity problem of a neutrino target area, where most of the available beam is required for most of the time.

15. REMAINING PROBLEMS

In spite of our extensive understanding of the radiation environment of proton accelerators there is still a great deal of work to be done. For radiation protection purposes we have all the means at our disposal to deal with the remanent activity hazards and the estimation of dose equivalent from neutrons less than 20 MeV. For the lower energy high-energy accelerators, the ^{11}C activation technique can estimate the DE from particles with energies greater than 20 MeV, but we do not have practical techniques of proven capability for particle spectra which extend to several hundred GeV. The complete particle spectrum at any accelerator is unknown. This is most embarrassing for protons in the region 10-100 MeV since these are recorded twice in personal dosimetry -- once with the $\beta\gamma$ badge and a second time (with significant overestimation of their dose) by neutron films. Since muons are minimum ionizing particles, muon dosimetry is no problem.

For shield design we have adequate models at our disposal for the hadron component, but we still do not know whether the physical models used in our muon transport calculations will stand the test of detailed experiments. This, to me, working at a 400 GeV accelerator, is the greatest uncertainty in our understanding of the radiation environment of proton accelerators.

Acknowledgements

In this review I take full responsibility only for the choice and ordering of the contents. I have quoted from many other reviews and am therefore duty-bound to gratefully acknowledge the contributions of all persons mentioned in the references. However, the un-referenced contributions by W.H. Barkas, P.H. Fowler, K. O'Brien and J. Ranft must be especially acknowledged.

Finally, I should like to thank M. Awschalom, K. Goebel, M. Höfert, J. Ranft, A. Rindi, J. Routti and R. Thomas for stimulating and maintaining my interest in this subject.

REFERENCES

- 1) Recommendations of the International Commission on Radiological Protection, ICRP-21 (1971).
- 2) G.R. Stevenson and K.B. Shaw, Conf. on Radiation Protection in Accelerator Environment, RHEL, 1969 (RHEL, Didcot, 1969), p. 19.
- 3) M. Tyren, Appebergs Baktrycheri AB, Uppsala (1958).
- 4) A. Ramakrishnan, Elementary particles and cosmic rays (Pergamon Press, Inc., NY, 1962), p. 400.
- 5) G. Ranft and J. Ranft, Univ. of Leipzig (DDR) report TUL 41 (1970).
- 6) H. Grote, R. Hagedorn and J. Ranft, Atlas of particle spectra (CERN, Geneva, 1970).
- 7) G. Cocconi, L.J. Koester and D.H. Perkins, UCRL 10022 (1962), p. 167.
- 8) G. Trilling, UCID 10148 (1966).
- 9) J. Ranft, CERN MPS/Int. MU/66-7 (1966).
- 10) J. Ranft and T. Borak, FNAL FN-193 (1969).
- 11) J. Ranft, CERN Lab II-RA/71-1 (1971).
- 12) J. Ranft, CERN Lab II-RA/75-2 (1975).
- 13) J. Ranft and J.T. Routti, Comput. Phys. Commun. 7, 327 (1974).
- 14) J. Ranft, CERN Lab II-RA/75-1 (1975).
- 15) N. Metropolis et al., Phys. Rev. 110, 185 and 204 (1958).
- 16) H.W. Bertini, CONF 691101 (1969), p. 42.
- 17) H.W. Bertini, M.P. Guthrie and A.H. Culkowski, ORNL-TM-3148 (1972).
- 18) N.B. Gove, H.W. Bertini, M. Feliciano and A.H. Culkowski, ORNL-TM-2627 (1971).
- 19) N. Bohr, Nature 137, 344 (1936).
- 20) V. Weisskopf, Phys. Rev. 52, 295 (1937).
- 21) I. Frenkel, Soviet Phys. 9, 533 (1936),
- 22) S.J. Lindenbaum, Annu. Rev. Nuclear Sci. 11, 213 (1961).
- 23) C. Passow, DESY Notiz A 2.85 (1962).
- 24) R.G. Alsmiller Jr., ORNL-TM-1298 (1965).

- 25) M. Barbier and R. Hunter, CERN 71-13 (1971).
- 26) K. O'Brien, CONF 691101 (1969), p. 253.
- 27) A. Citron, L. Hoffmann, C. Passow, W.R. Nelson and M. Whitehead, Nuclear Instrum. Methods 32, 48 (1965).
- 28) K. O'Brien and J.E. McLaughlin, Nuclear Instrum. Methods 60, 129 (1968).
- 29) T.W. Armstrong, R.G. Alsmiller Jr., K.C. Chandler and B.L. Bishop, ORNL-TM-3667 (1972).
- 30) A. Van Ginneken, FNAL-FN-250 (1972).
- 31) J. Ranft, Particle Accelerators 3, 129 (1972).
- 32) J. Ranft and J.T. Routti, CERN Lab II-RA/71-4 (1971).
- 33) J. Ranft and J.T. Routti, CERN Lab II-RA/72-8 (1972).
- 34) J. Ranft, CERN Lab II-RA/73-2 (1973).
- 35) G.R. Stevenson, D.M. Squier and G.S. Levine, RHEL/MR7 (1971).
- 36) J.T. Routti, TKK-F-A222 (1973).
- 37) J. Ranft and G.R. Stevenson, to be published.
- 38) The 300 GeV Programme, CERN 1050 (1972), p. 129.
- 39) W.S. Gilbert et al., UCRL-17941 (1968).
- 40) K. Goebel and J. Ranft, CONF 691101 (1969),
- 41) G.R. Stevenson et al., RHEL-M/148 (1969).
- 42) J.T. Routti, CONF 691101 (1969),
- 43) K.B. Shaw, G.R. Stevenson and R.H. Thomas, Health Physics 17, 459 (1969).
- 44) W.N. Hess, H.W. Patterson and R. Wallace, Phys. Rev. 116, 445 (1959).
- 45) T.W. Armstrong, K.C. Chandler and J. Barish, ORNL-4800 (1972), p. 63.
- 46) A. Rindi and R.H. Thomas, Annu. Rev. Nuclear Sci. 23, 315 (1973).
- 47) H.A. Wright et al., Health Physics 16, 13 (1969).
- 48) D. Thériot, FNAL-TM-229 (1970).
- 49) D. Thériot, FNAL-TM-260 (1970).
- 50) C. Richard-Serre, CERN 71-18 (1971).

- 51) H. Atherton, private communication.
- 52) J. Ranft and E. Freytag, CERN 71-21 (1971), p. 47.
- 53) D. Keefe and C.M. Noble, UCRL-18117 (1968).
- 54) R.J. Riddell Jr., UCRL-11989 (1965).
- 55) R.G. Alsmiller Jr., F.S. Alsmiller, J. Barish and Y. Shima, CERN 71-16 (1971), p. 601.
- 56) G.R. Stevenson and D.M. Squier, Health Physics 24, 87 (1973).
- 57) K. Goebel, G.R. Stevenson, J.T. Routti and H.G. Vogt, CERN Lab II-RA/Note/75-10 (1975).
- 58) A. Rindi and R.H. Thomas, LBL-3322 (1975).
- 59) G.R. Stevenson, CERN Lab II-RA/Note/72-10 (1972).
- 60) E. Bruninx, CERN 61-1 (1961).
- 61) G. Rudstam, Z. Naturforschung 21a, 1027 (1966).
- 62) M. Barbier, Induced Radioactivity (North-Holland Publ. Co., 1969).
- 63) T.W. Armstrong, J. Geophys. Res. 74, 1361 (1969).
- 64) T.W. Armstrong and R.G. Alsmiller Jr., Nuclear Sci. Engng. 38, 53 (1969).
- 65) K. Goebel, J. Ranft and G.R. Stevenson, CERN 71-21 (1971), p. 101.
- 66) A.H. Sullivan and T.W. Overton, Health Physics 11, 1101 (1965).
- 67) T.W. Armstrong and J. Barish, ORNL-TM-2583 (1969).
- 68) K. Goebel and J. Ranft, CERN 70-16 (1970).
- 69) G.R. Stevenson, CERN Lab II-RA/Note/73-17 (1973).
- 70) M. Höfert, F. Coninx, J.M. Hanon and C. Steinbach, CERN DI/HP/185 (1975).
- 71) T.W. Armstrong and J. Barish, Nuclear Sci. Engng. 40, 128 (1970).
- 72) W.S. Gilbert, K. Goebel, H.W. Patterson and A.R. Smith, UCRL-19368 (1969).
- 73) D. Nachtigall and S. Charalambus, CERN 66-28 (1966).
- 74) A. Rindi and G.R. Stevenson, CERN Lab II-RA/Note/73-3 (1973).
- 75) J. Tuyn, CERN/NP/73-131 (1973).
- 76) A. Van Ginneken, FNAL-TM-630 (1975).

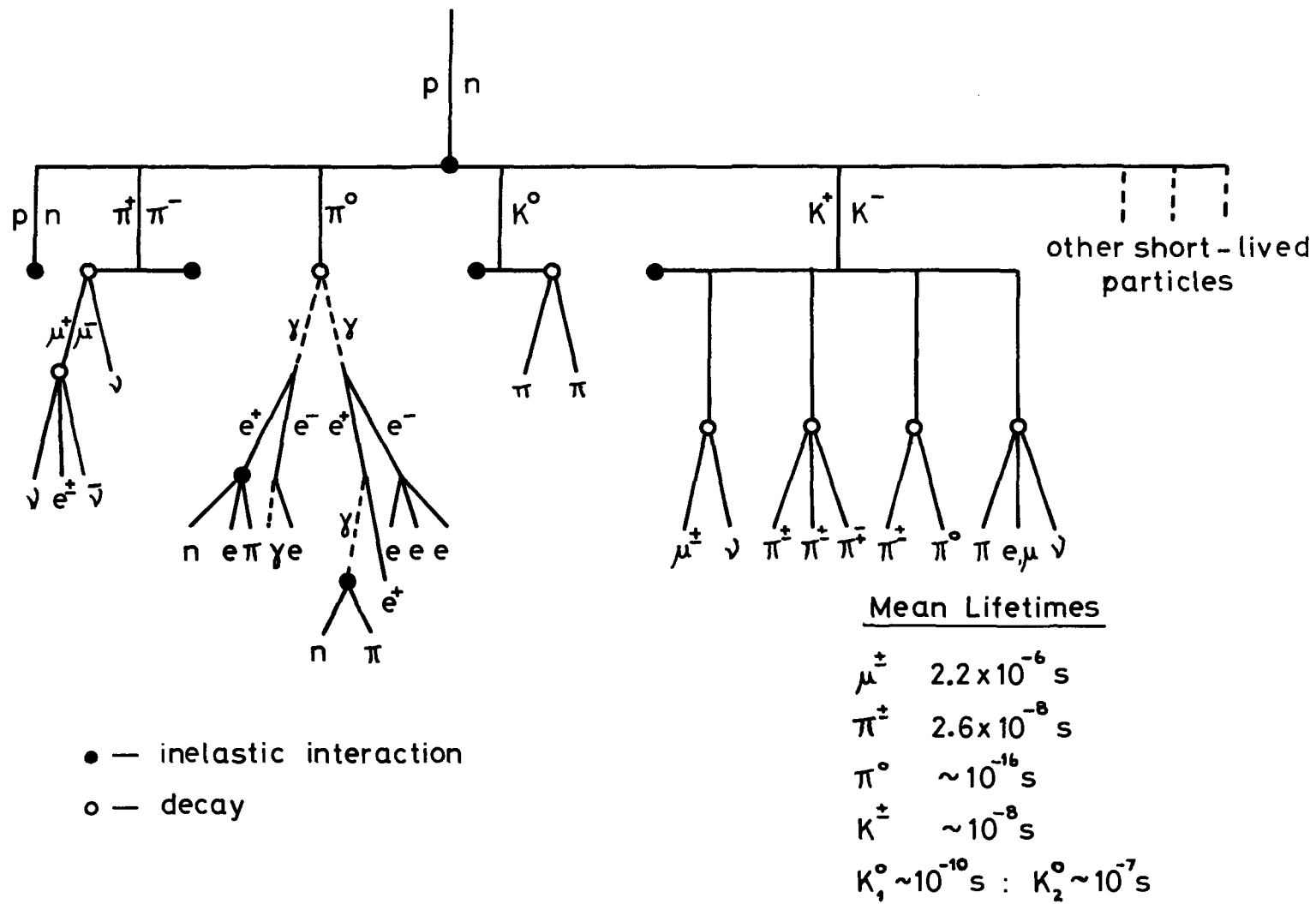


Fig. 1 Schematic cascade.

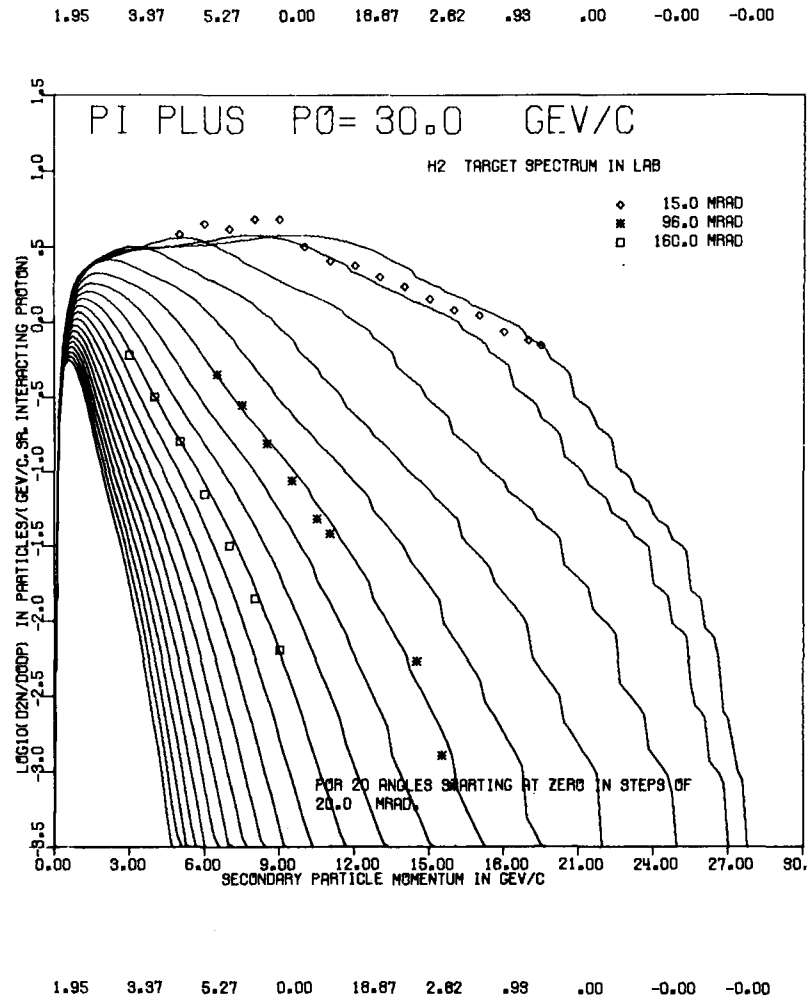


Fig. 2 Secondary π^+ spectrum from 30 GeV/c pp-collision⁶⁾.

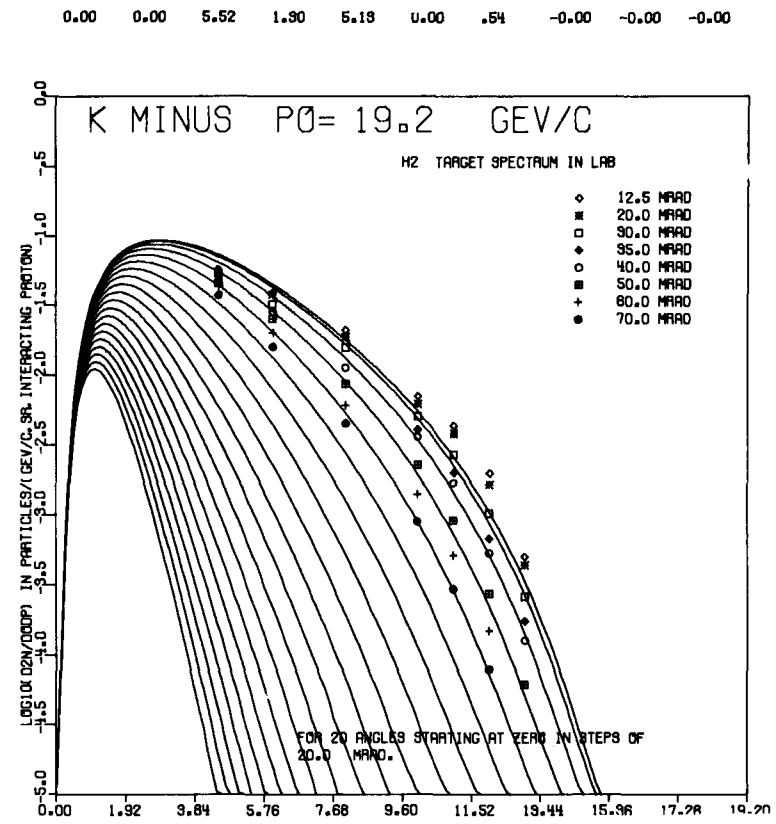


Fig. 3 Secondary K^- spectrum from 19.2 GeV/c pp-collision⁶⁾.

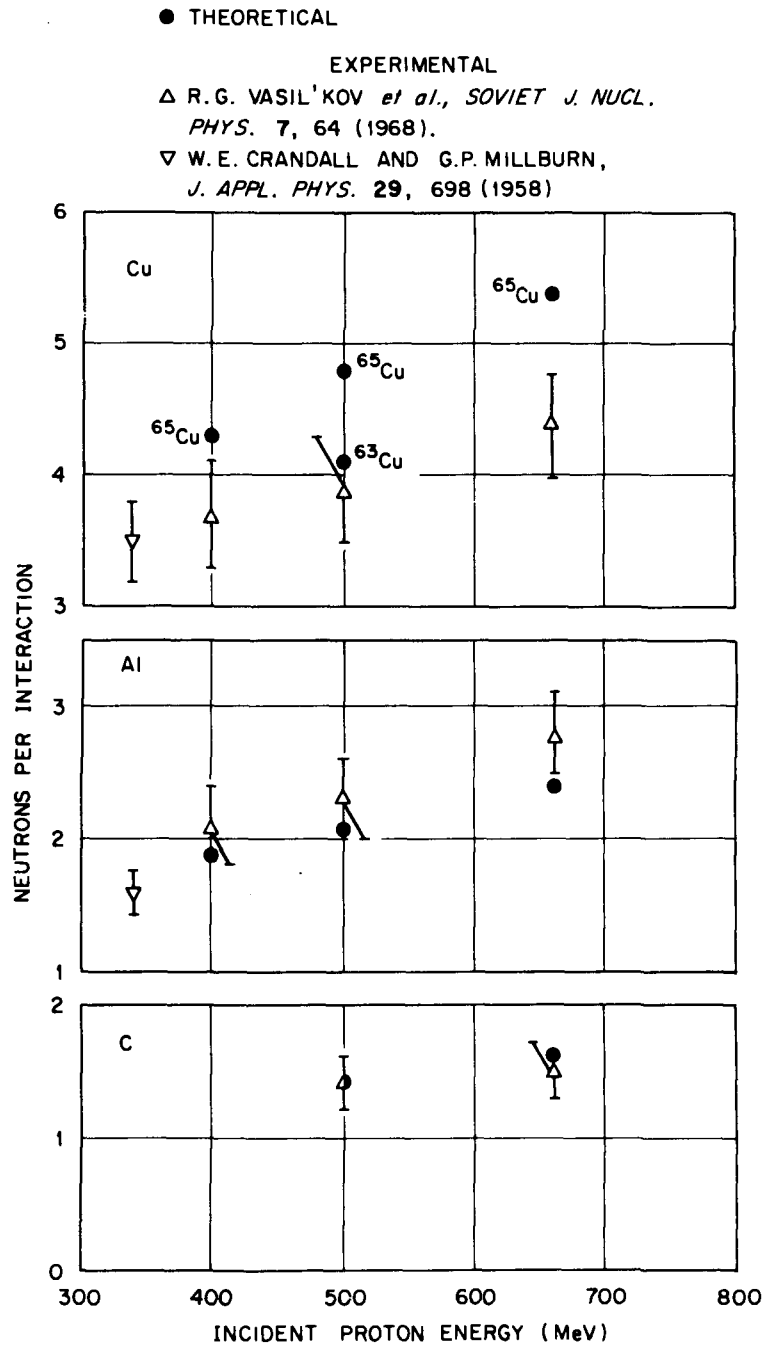


Fig. 4 The average number of neutrons emitted per interaction of protons with carbon, aluminium and copper¹⁷⁾. Where error bars are not indicated they are smaller than the symbols.

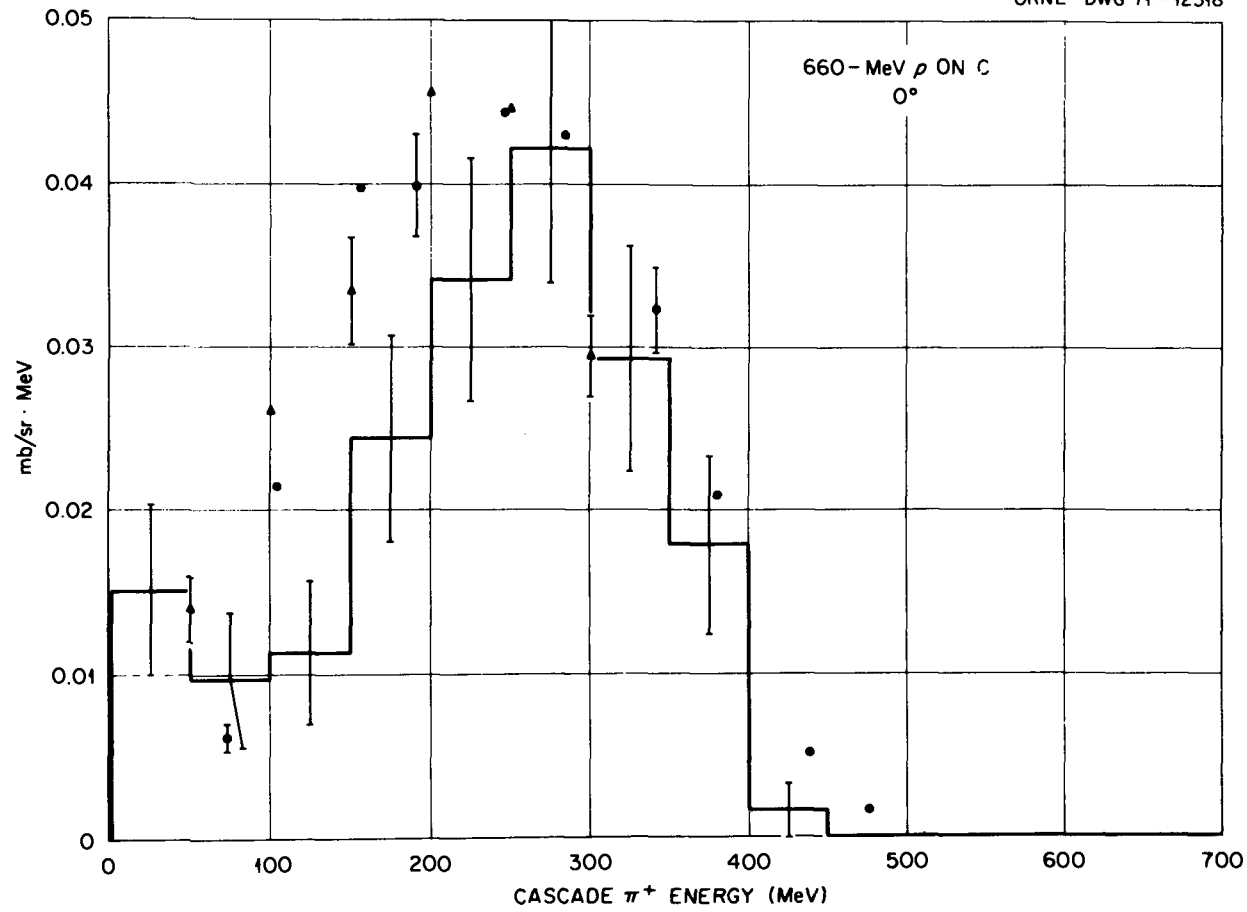


Fig. 5 Energy spectra of π^+ emitted at 0° from 660 MeV protons on carbon¹⁷⁾. Experimental data: ● Haddock et al., UCLA-34P106, 725 MeV; ▲ Hirt et al., CERN 69-24, 600 MeV. Histogram: theoretical results for the angular interval $0-10^\circ$.

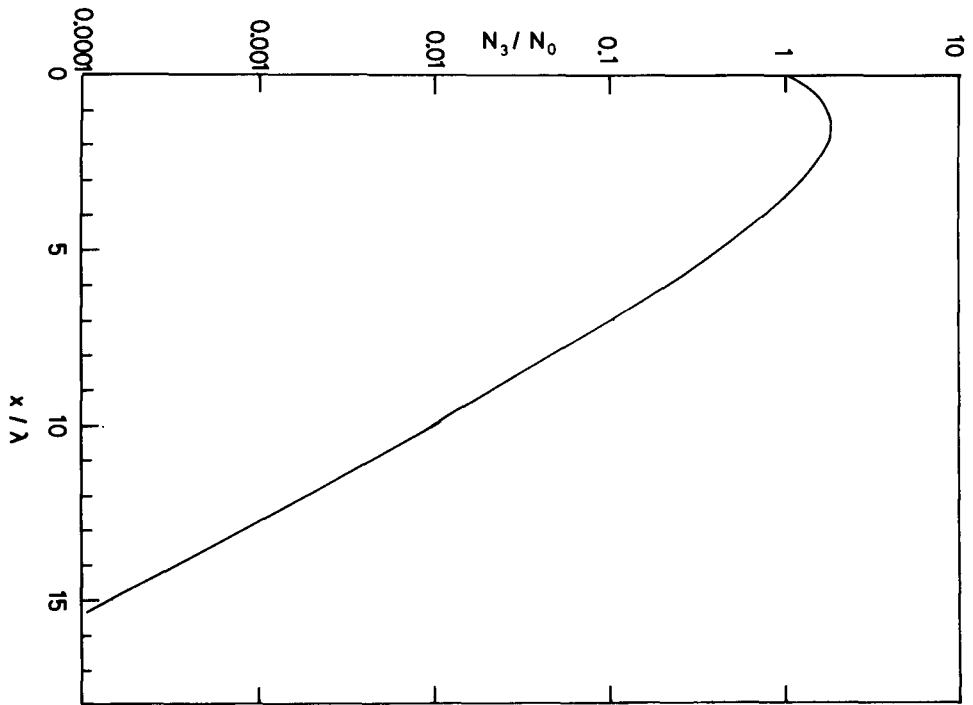


Fig. 6 Development of a one-dimensional cascade;
 $n = 3$, $m = 2$.

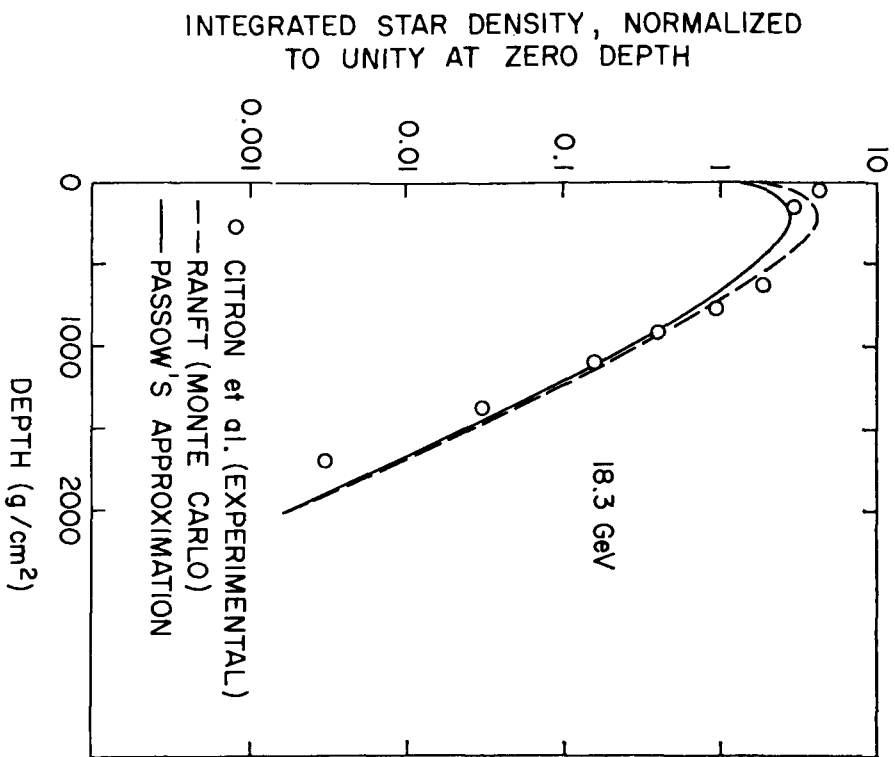


Fig. 7 Variation of the laterally integrated star density in nuclear emulsion with depth of a cascade produced by an 18.3 GeV proton beam normally incident on an iron slab²⁶⁾. The measurements were made by Citron et al.²⁷⁾.

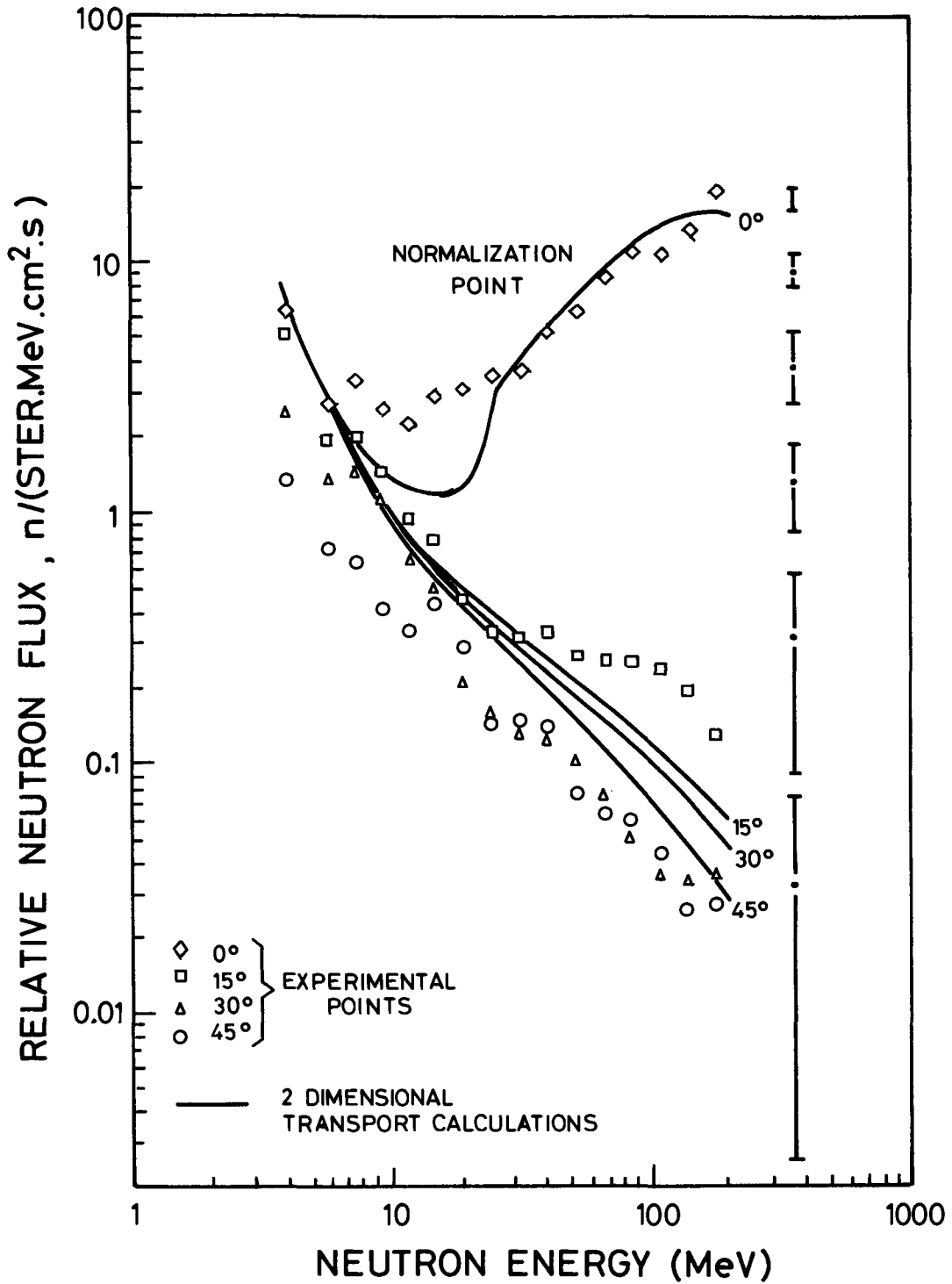


Fig. 8 Experimental and theoretical determination of the distribution of neutrons in energy and angle per steradian emerging from a 40 cm iron slab irradiated by a gun source made from the 49° neutron beam of the Princeton-Pennsylvania Accelerator. The error bars at the right of the graph are roughly the same size for a given ordinate. Calculations are performed for the centre of the neutron distribution, $r = 0$ ²⁸).

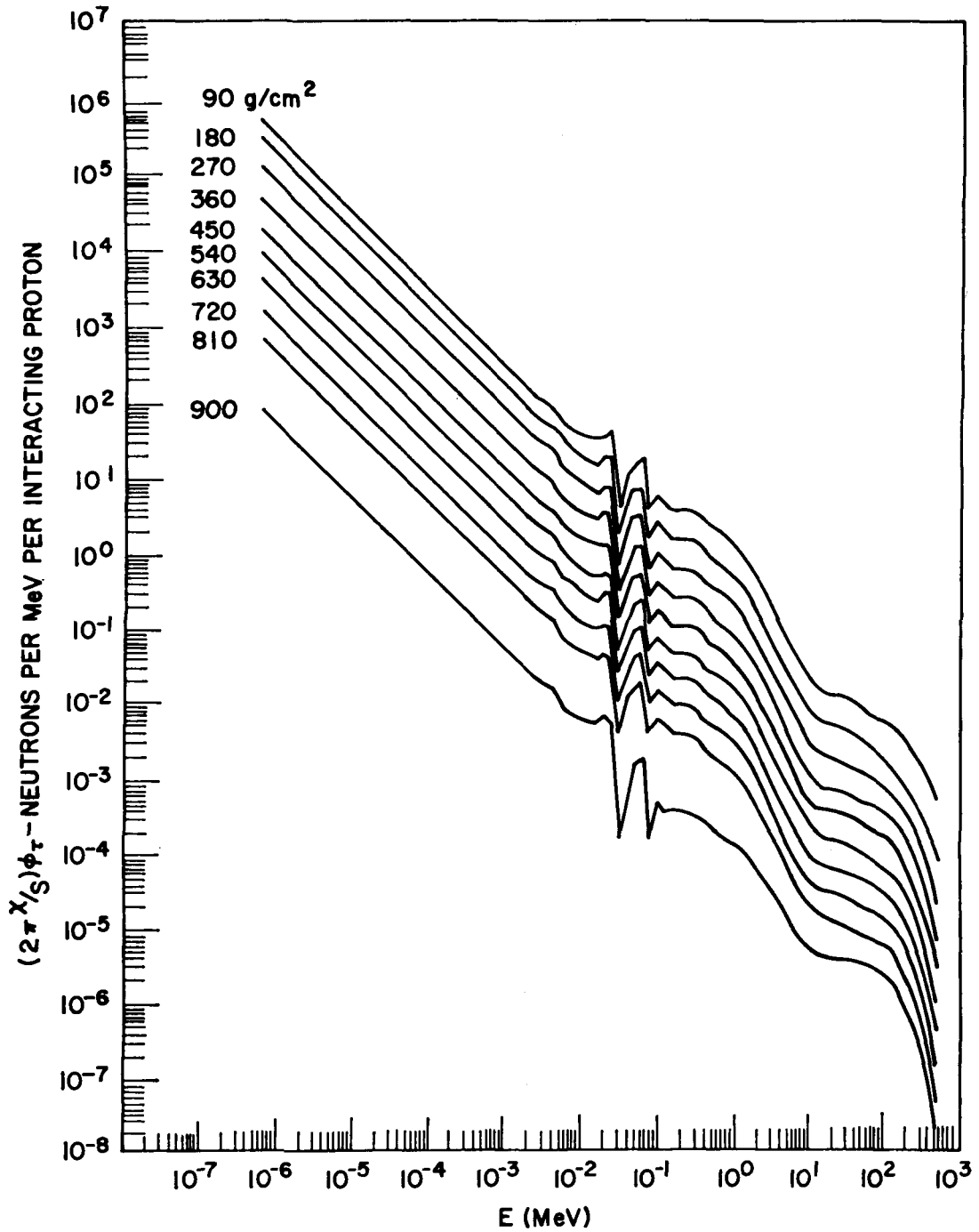


Fig. 9 Neutron fluxes in a 900 g/cm^2 thick simulated heavy concrete shield of a 3 GeV proton synchrotron, as a function of energy and position in the barrier²⁸).

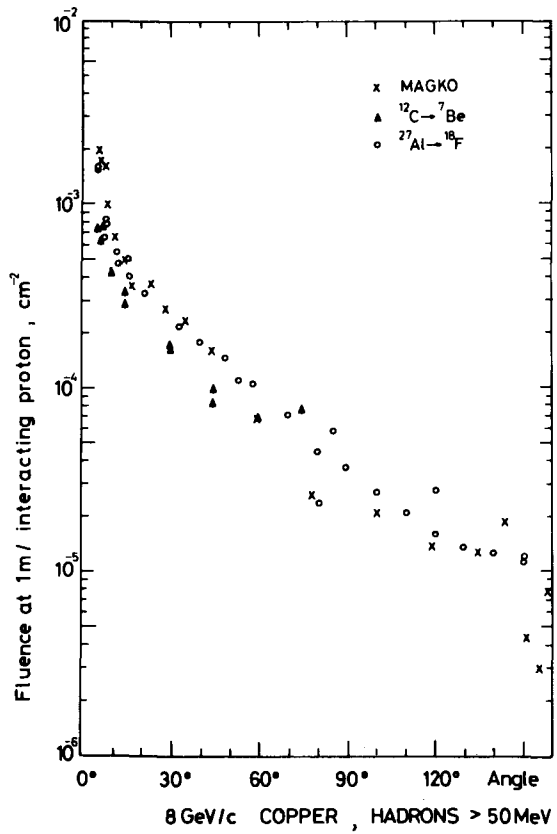


Fig. 10 Hadron yield from 8 GeV/c proton on copper interactions³⁷⁾.

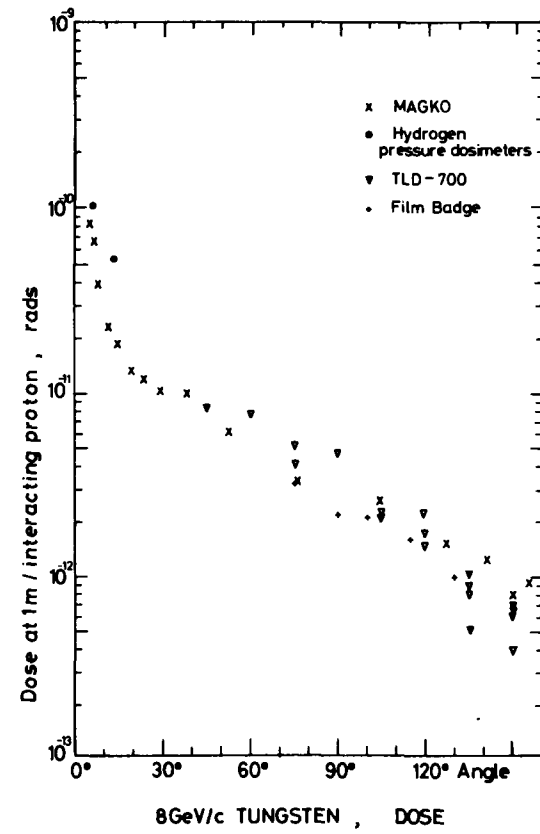


Fig. 11 Dose yield from 8 GeV/c proton on tungsten interactions³⁷⁾.

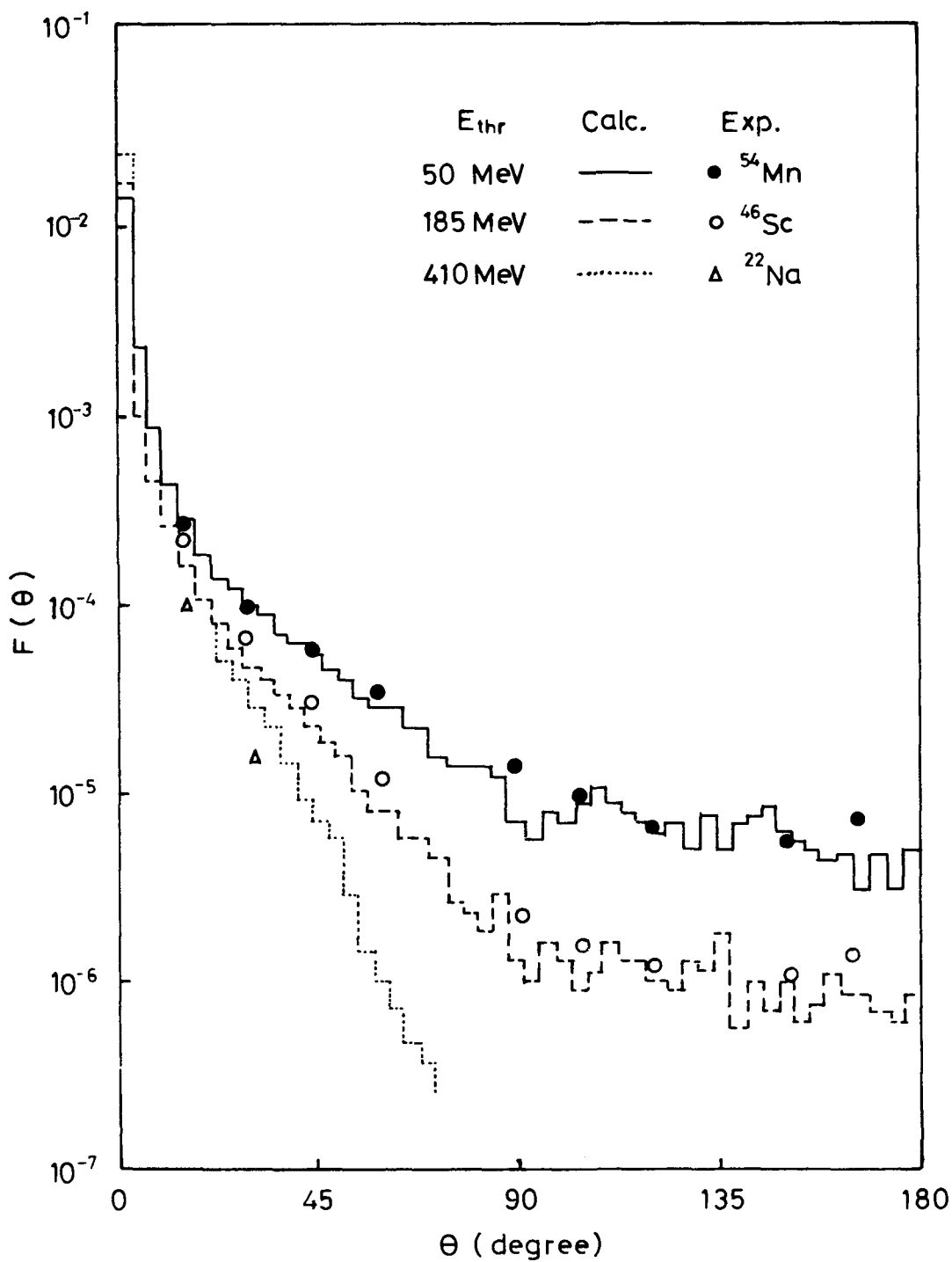


Fig. 12 Angular yield distributions³⁶⁾.

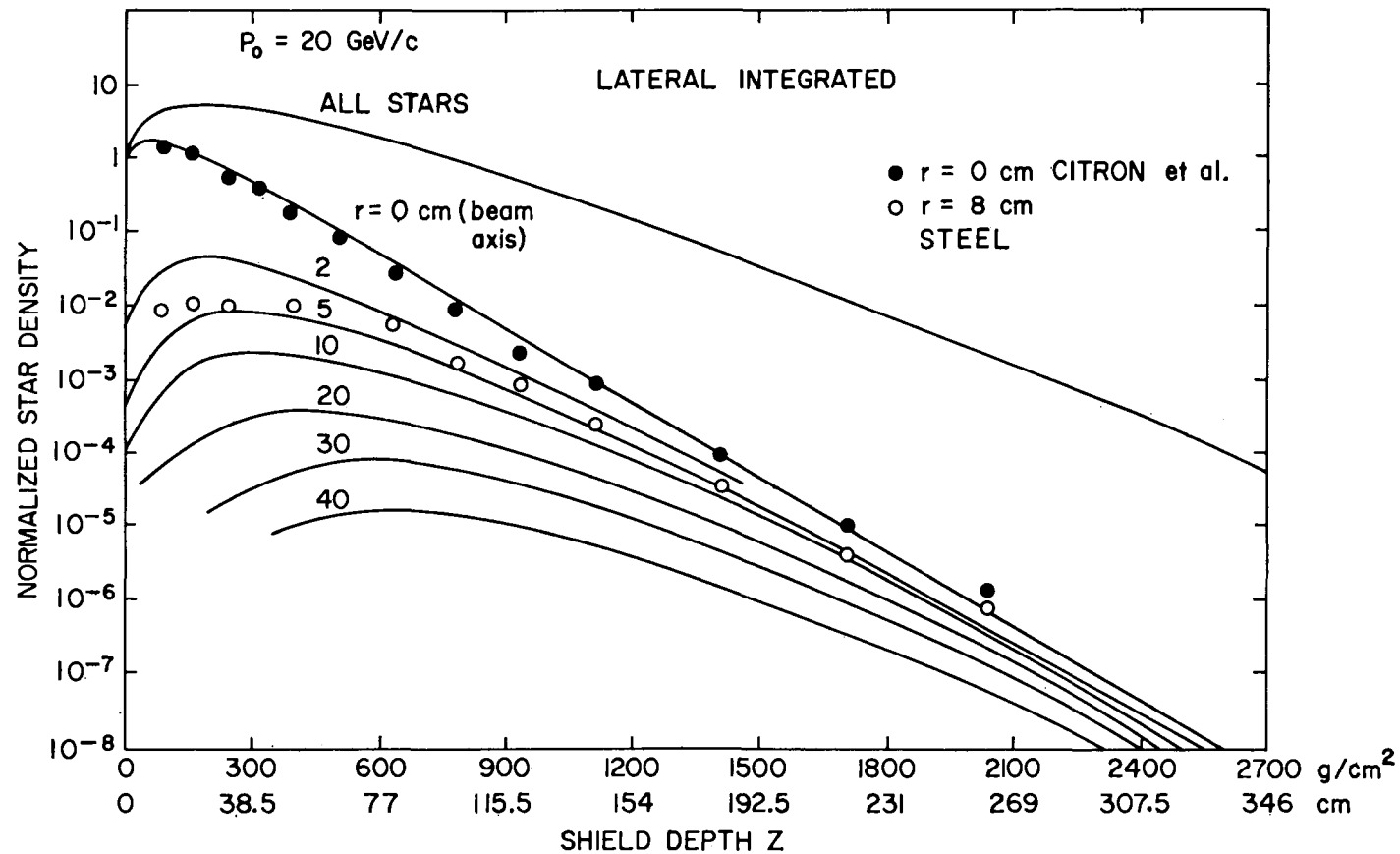


Fig. 13 The longitudinal development of the total star density (sum of proton, neutron, and pion star densities) for a cascade initiated by a well collimated proton beam of cross-section $10 \times 10 \text{ mm}^2$ and momentum $p_0 = 20 \text{ GeV/c}$ in steel³¹). The curves are normalized to unit proton star density at $r = 0$. The points represent the star densities along the beam axis ($r = 0$) and 8 cm outside the beam axis ($r = 8 \text{ cm}$) which were measured by Citron et al.²⁷).

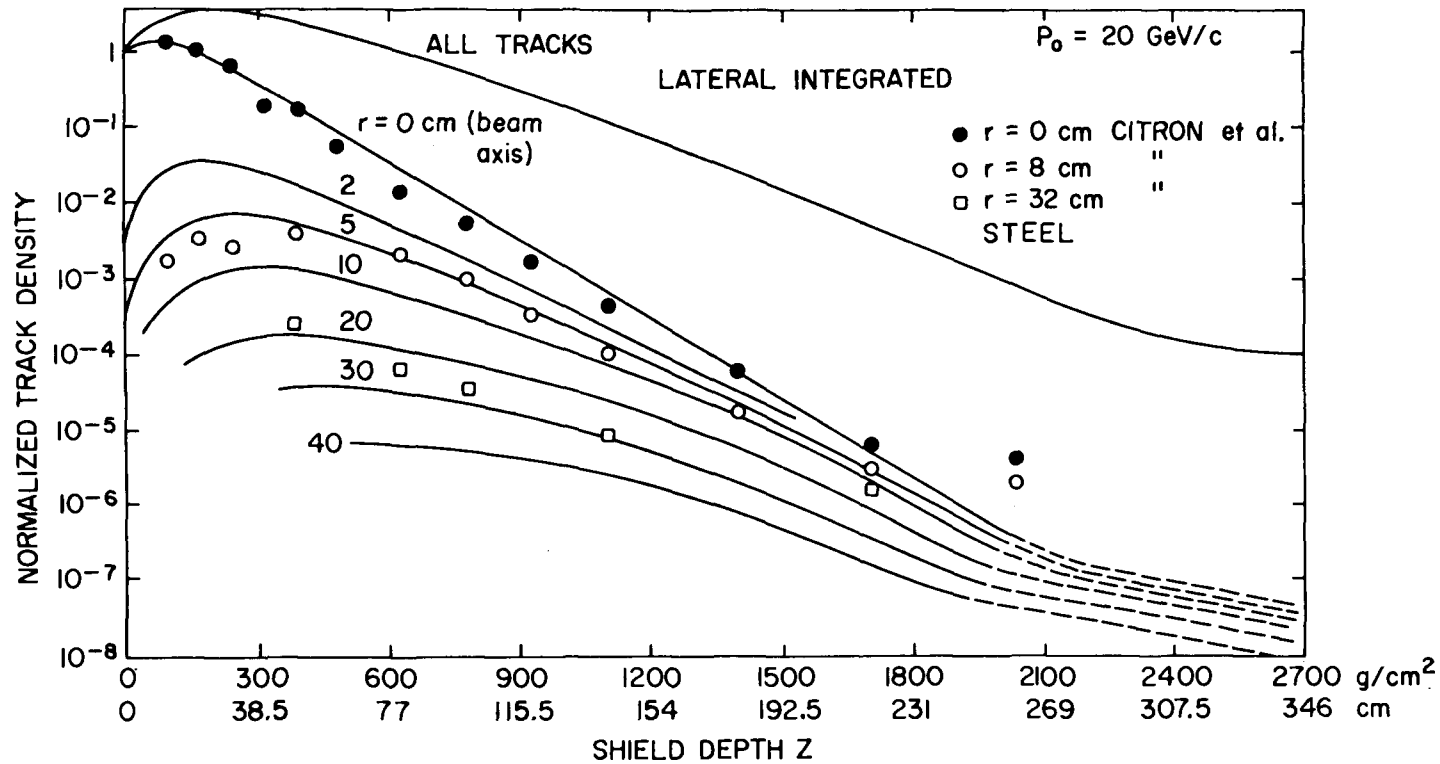


Fig. 14 The longitudinal development of the total track density (sum of proton, pion and muon track densities) for a cascade initiated by a well collimated proton beam of cross-section $10 \times 10 \text{ mm}^2$ and momentum $p_0 = 20 \text{ GeV}/c$ in steel³¹). The curves are normalized to unit proton track density at $r = 0$ and $z = 0$. The points represent the track densities along the beam axis ($r = 0 \text{ cm}$) and 8 and 32 cm outside the beam axis ($r = 8, 32 \text{ cm}$), which were measured by Citron et al.²⁷). The change in the slope of the curves near the depth $z = 2000 \text{ g}/\text{cm}^2$ arises from the muon track density.

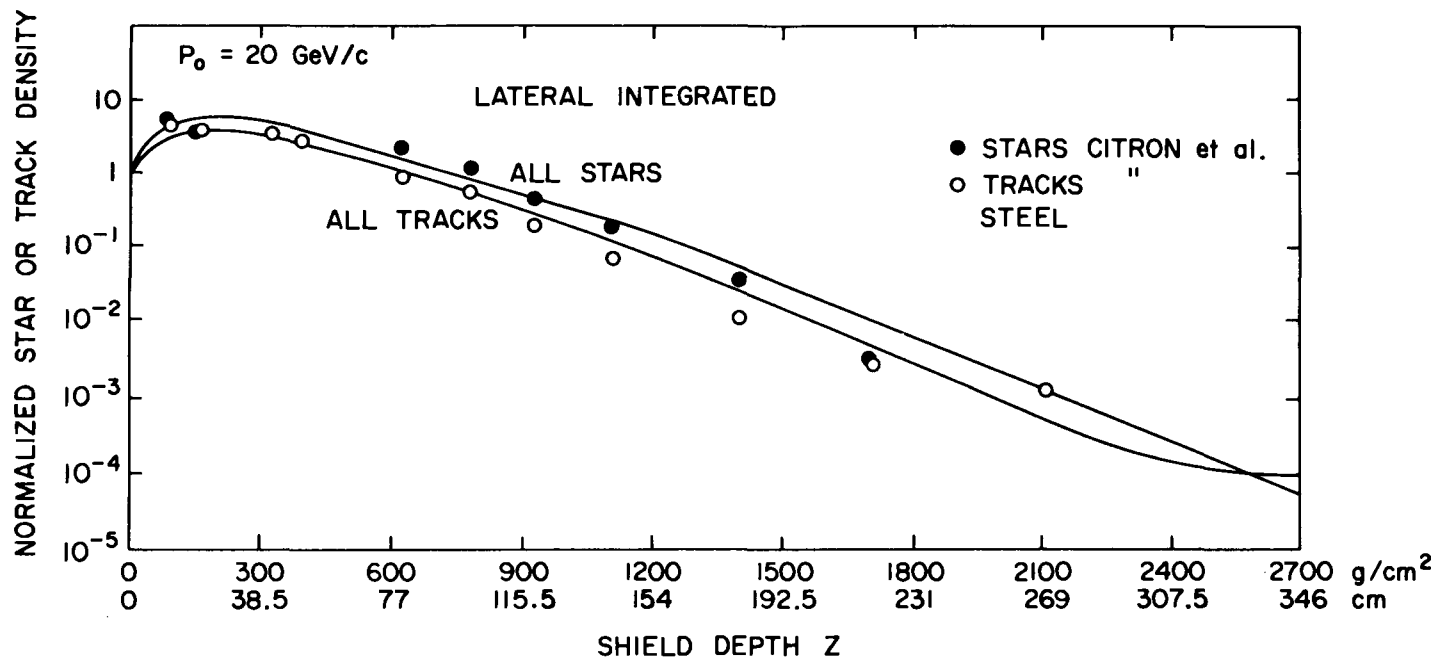


Fig. 15 Laterally integrated total star and total track density for a cascade initiated by a well collimated proton beam of momentum $p_0 = 20 \text{ GeV/c}$ in steel³¹⁾. The points represent the experimental integrated track and star densities which were given by Citron et al.²⁷⁾.

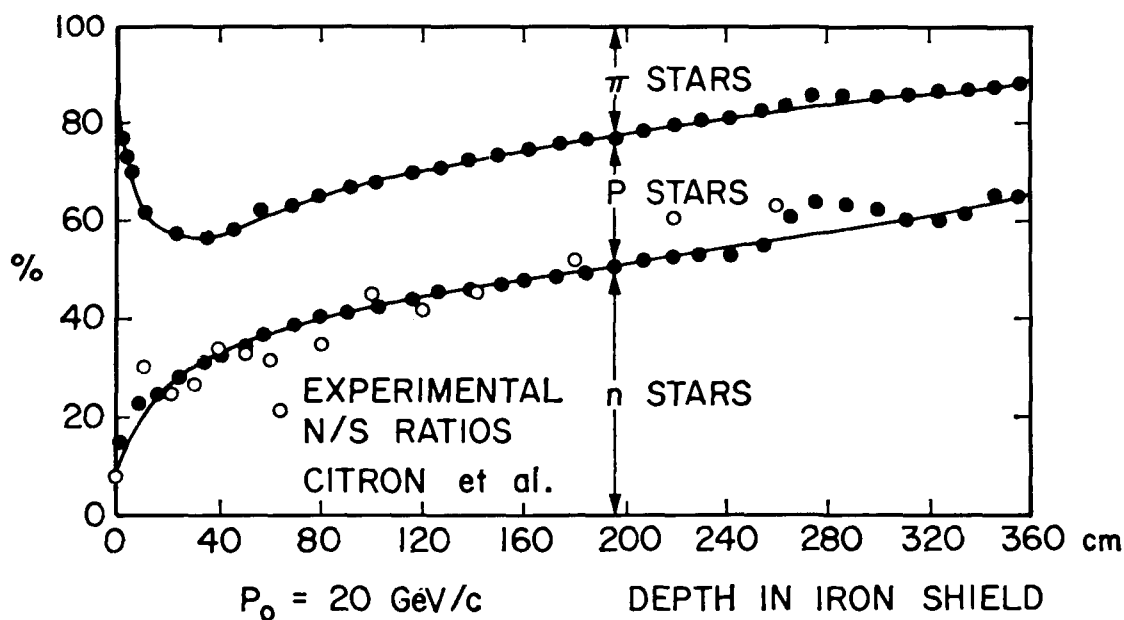


Fig. 16 Percentage of neutron, proton, and pion stars contributing to the total star density of a cascade initiated by a proton beam of $p_0 = 20$ GeV/c as function of the depth z in the shield³¹⁾. At $z = 0$ nearly 100 per cent of the stars are proton stars. The fraction of pion stars reaches a maximum of 45 per cent at $z = 30$ cm and decreases with z . The fraction of neutron stars increases steadily and reaches 60 per cent at about $z = 300$ cm. The points give the percentage of stars without primary track in the backward hemisphere (N/S) as measured by Citron et al.²⁷⁾. This represents a lower limit for the fraction of neutron stars.

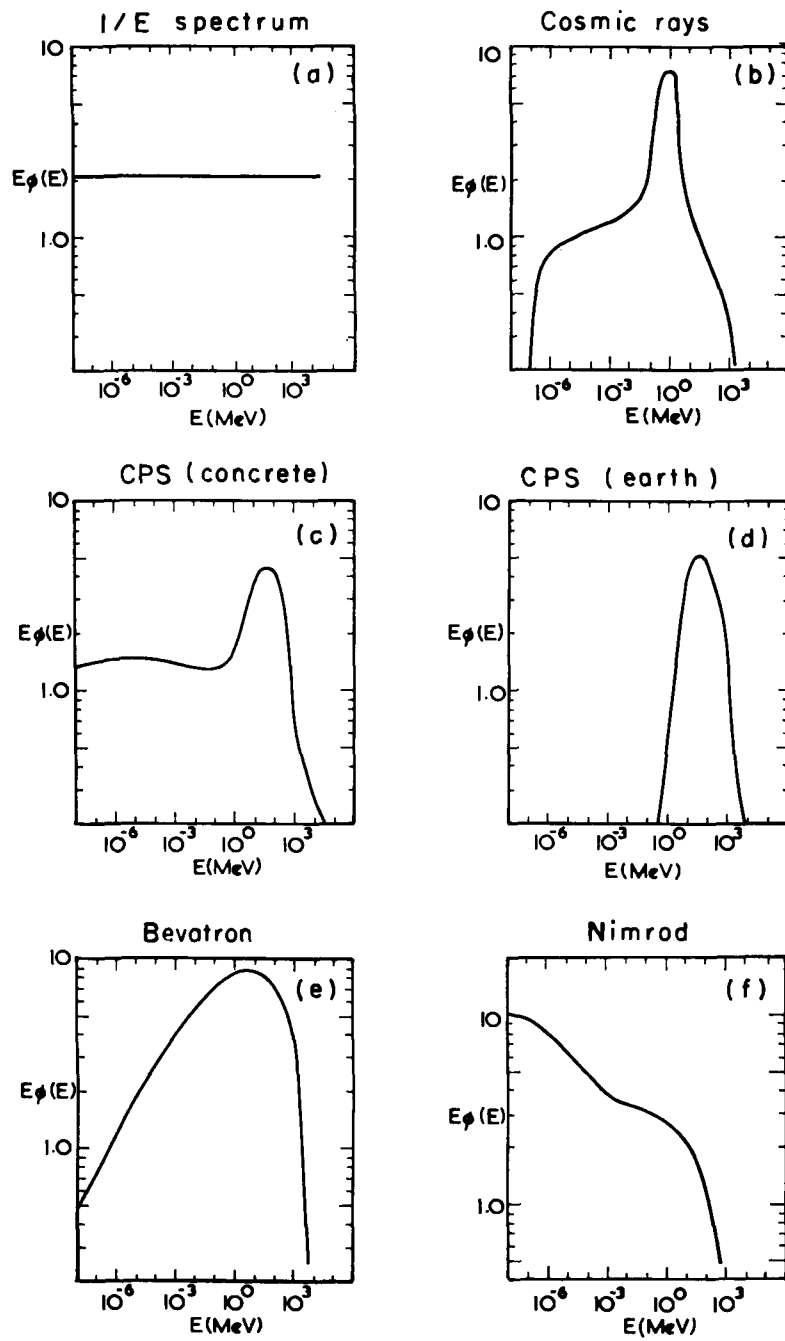


Fig. 17 Neutron spectra typical of those to be found outside the shields of proton synchrotrons.

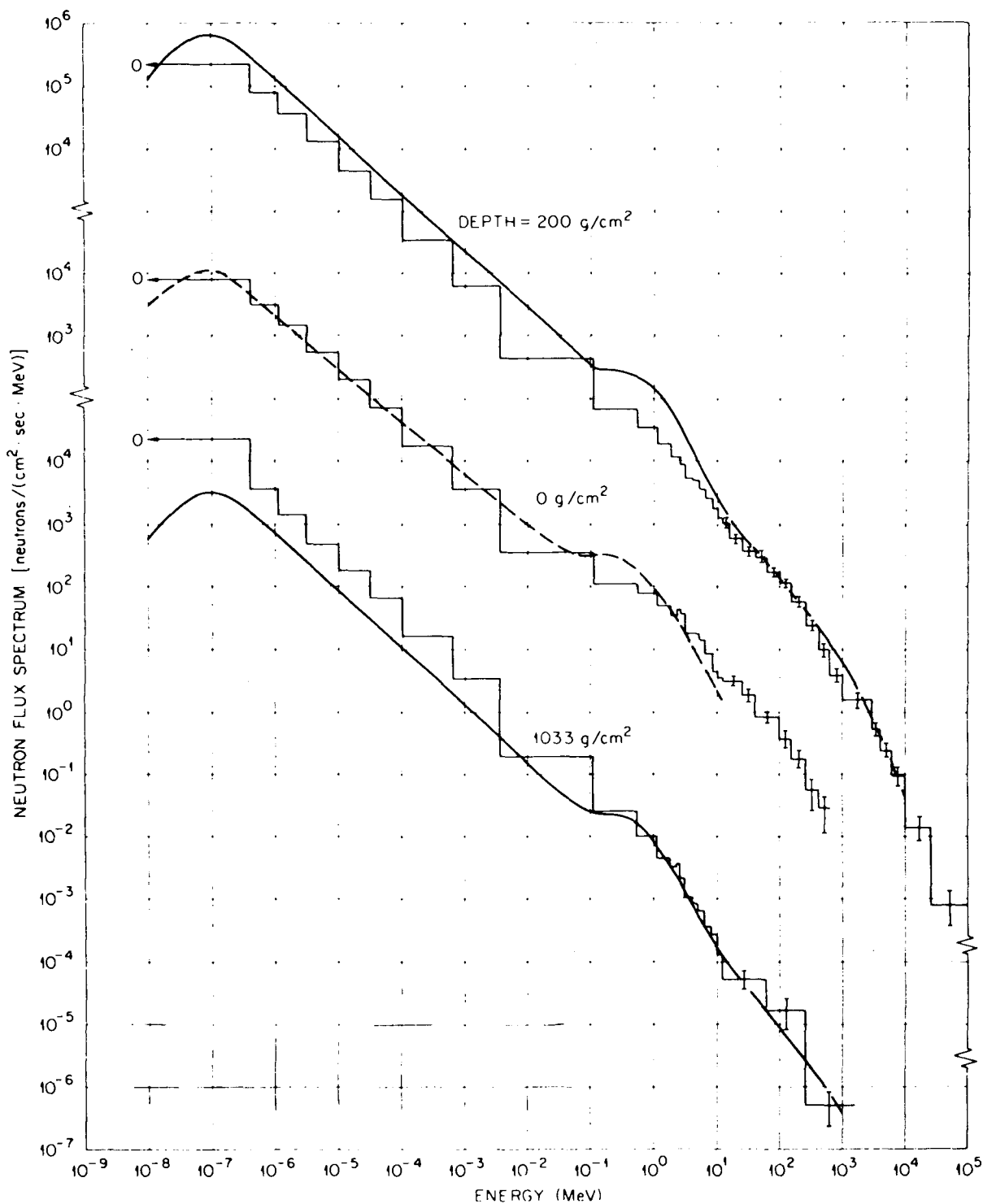


Fig. 18 Histograms show calculated values of the cosmic-ray neutron spectra due to Armstrong et al.⁴⁵⁾ which are compared with the measurements of Hess et al.⁴⁴⁾ (solid line) at depths in the atmosphere of 200 g/cm² and 1033 g/cm² and are also compared with calculations of Lingenfelter -- quoted by Armstrong et al.⁴⁵⁾ -- at the top of the atmosphere (dotted lines). The calculations and measurements are made in the range of geomagnetic latitudes 40-44° (from Ref. 46).

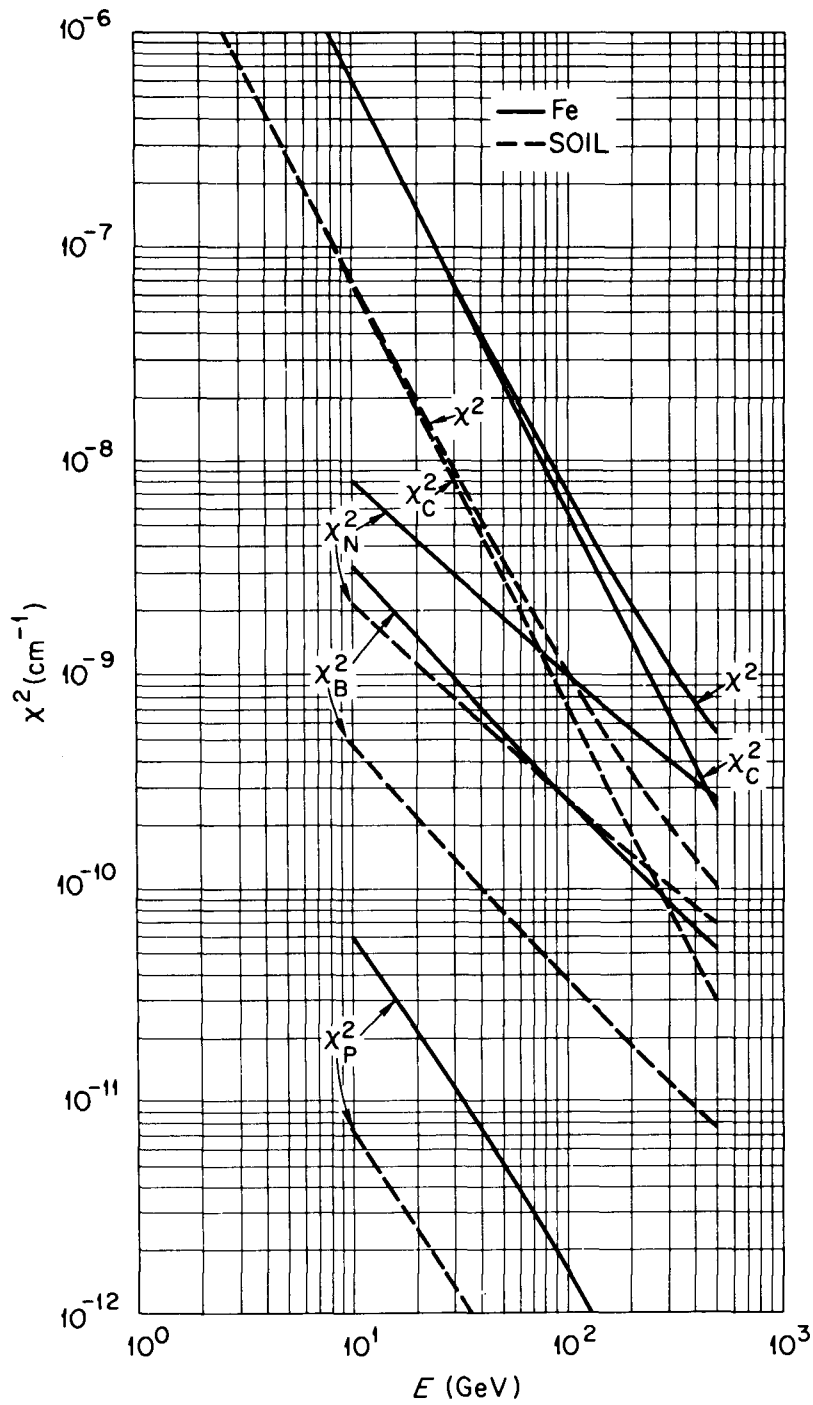


Fig. 19 One-fourth the mean-square scattering angle per unit distance versus muon energy. Also shown are the contributions from the various physical processes considered in calculating the mean-square scattering angle⁵⁵).

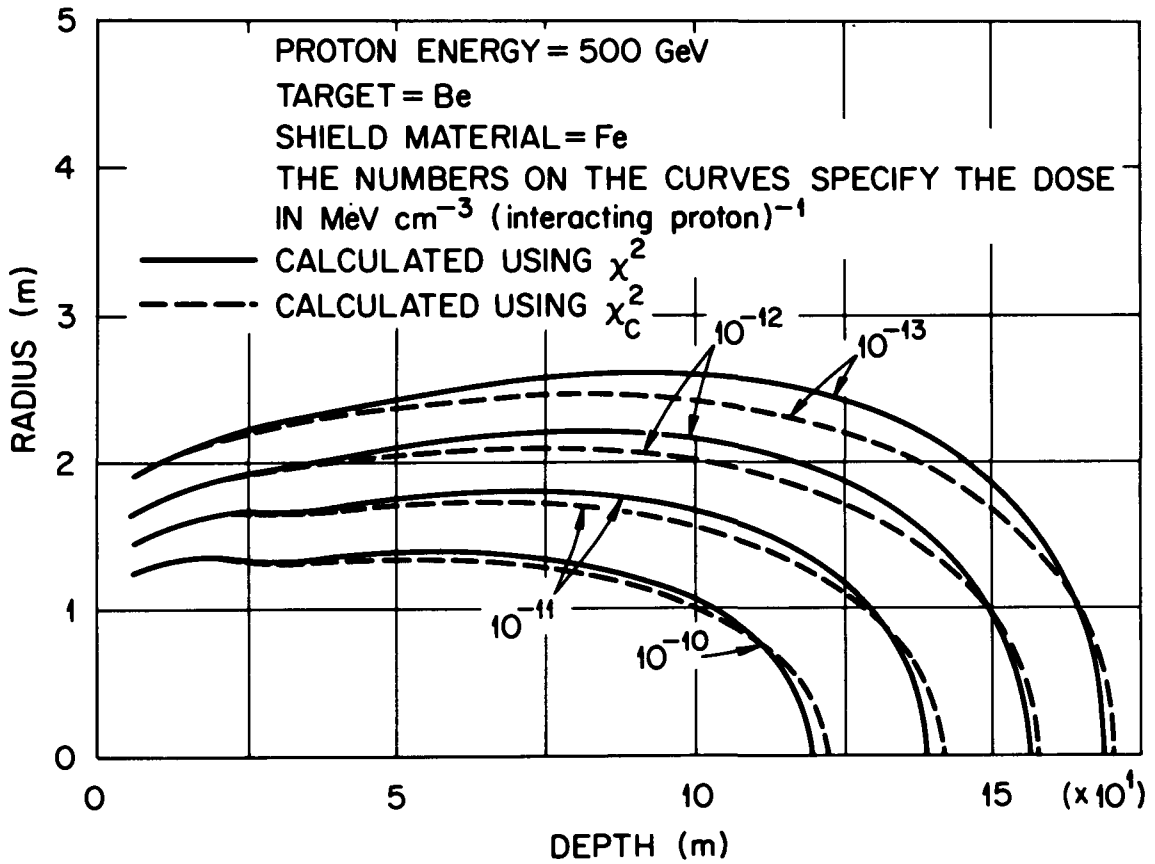


Fig. 20 Muon isodose contours in a soil shield for 500 GeV protons incident on a beryllium target⁵⁵).

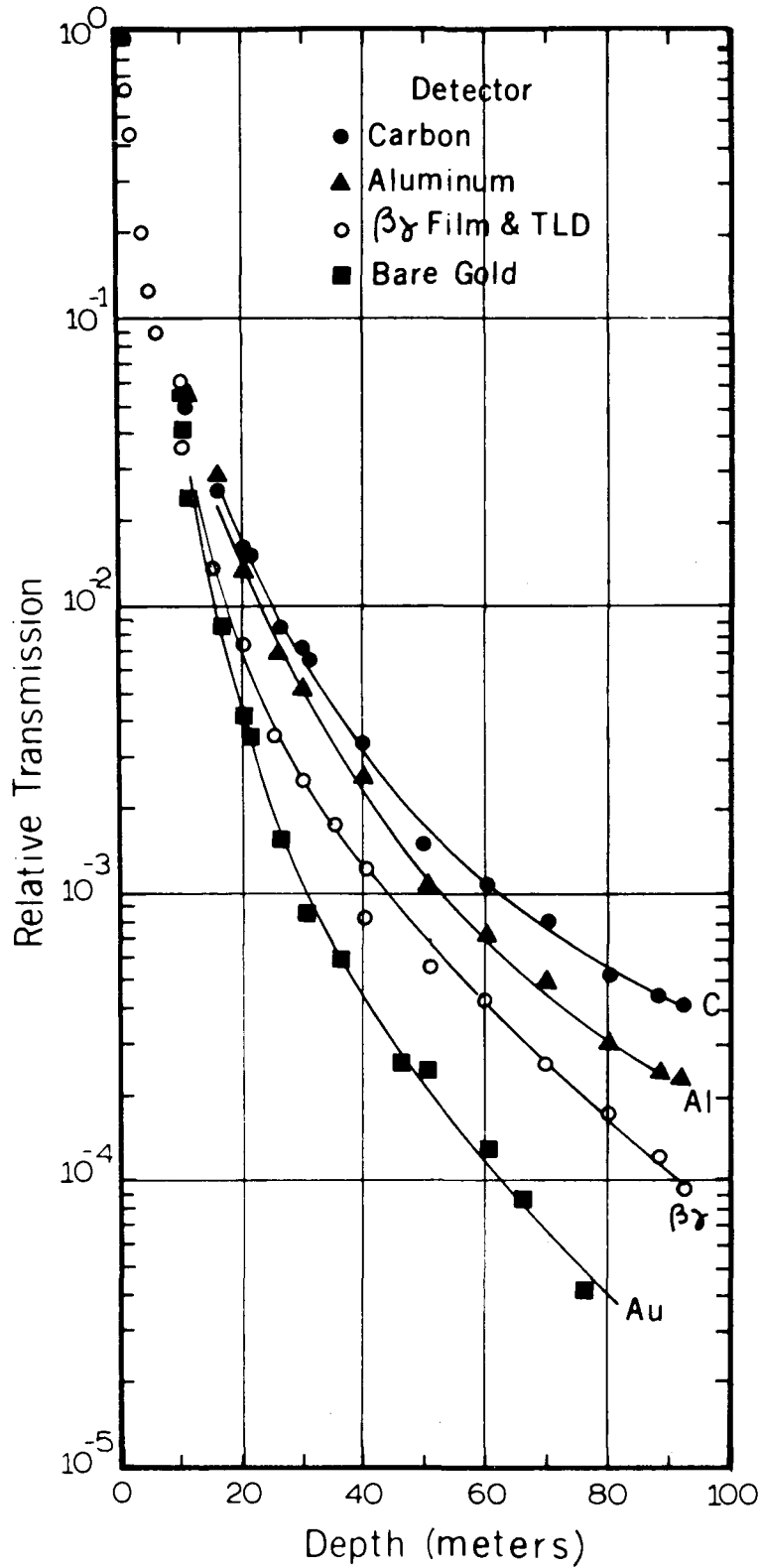


Fig. 21 Flux attenuation in the $1.8 \times 2.8 \text{ m}^2$ tunnels of the CERN PS ³⁹⁾.

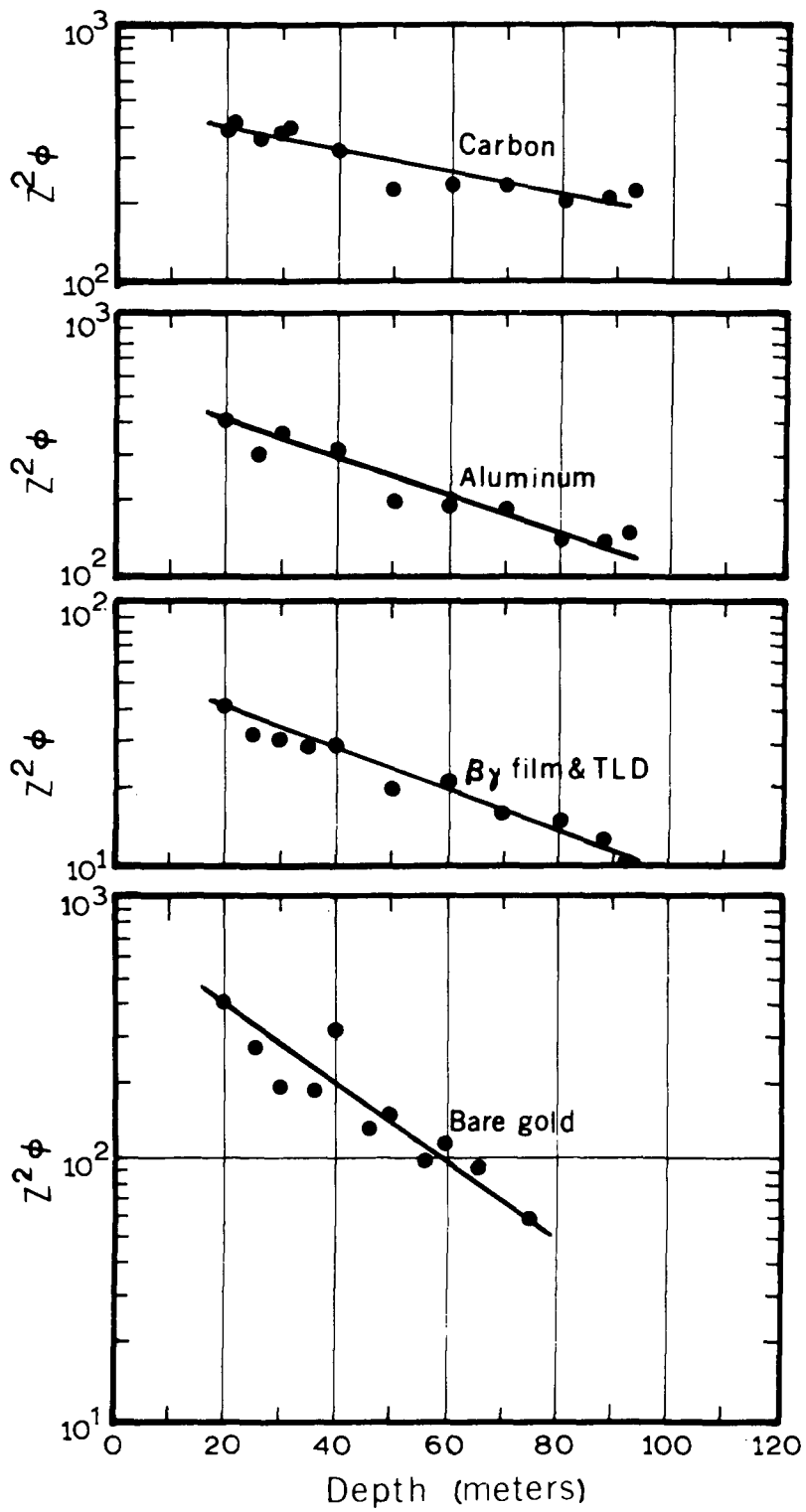


Fig. 22 Exponential absorption in the $1.8 \times 2.8 \text{ m}^2$ tunnels of the CERN PS for several detectors³⁹⁾.

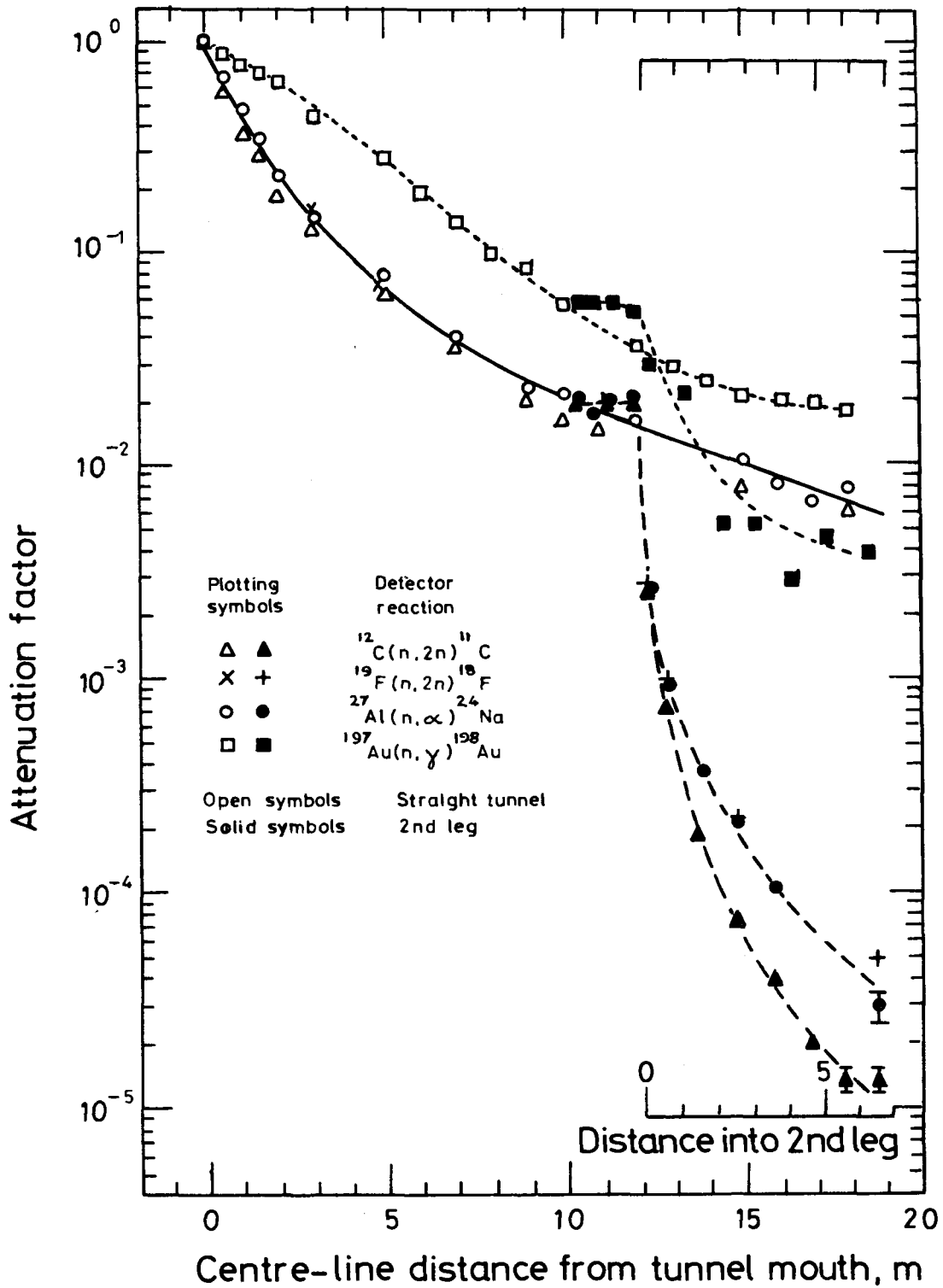


Fig. 23 Attenuation curves measured with activation detectors in a $2.3 \times 2.3 \text{ m}^2$ tunnel⁵⁶). Solid line: inverse square dependence modified by exponential term. Broken line: fits by eye to the data.

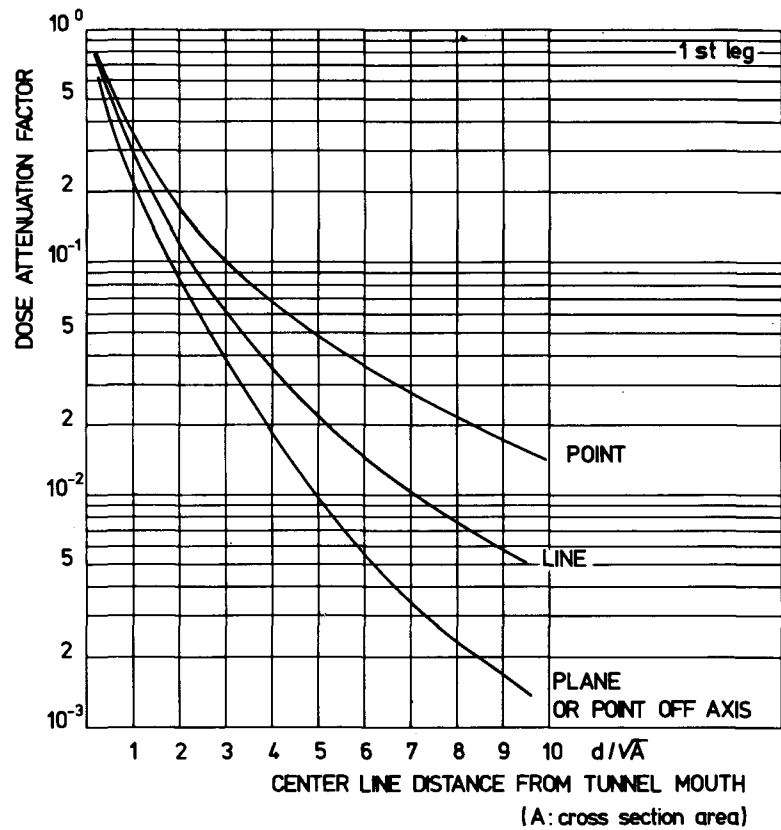


Fig. 24 Universal attenuation curves for the first leg of a tunnel.

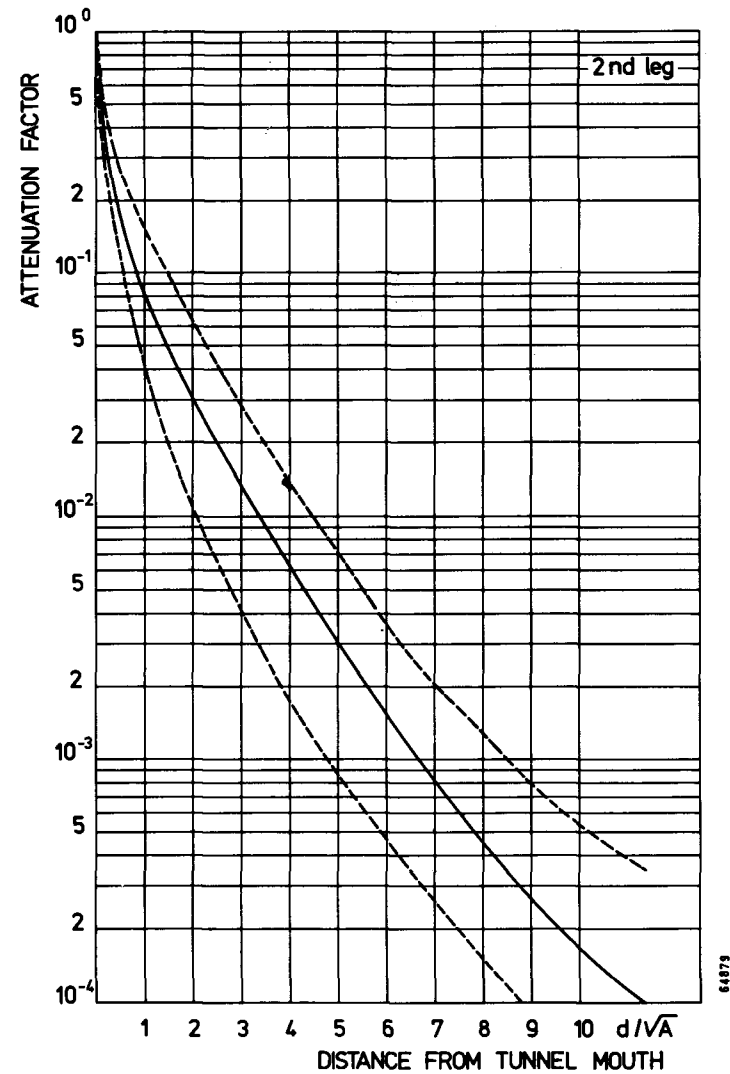


Fig. 25 Universal attenuation curves for the second leg of a tunnel.

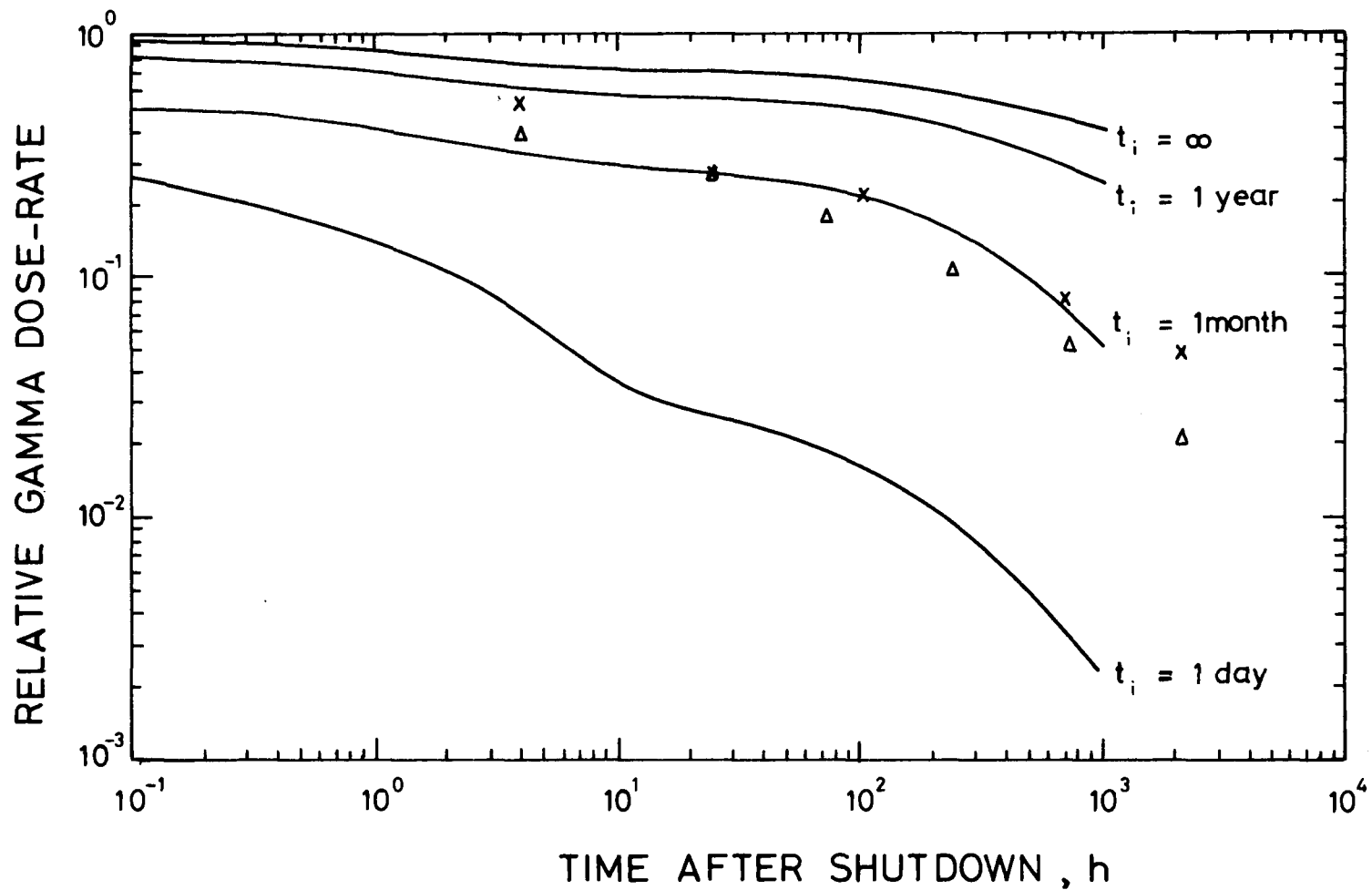


Fig. 26 Relative photon dose-rate from an iron block as a function of time after shut-down and irradiation time⁶⁵⁾. $E_0 = 3 \text{ GeV}$, radius of block 40 cm. Solid lines, calculation⁶⁴⁾; x experiment; Δ empirical⁶⁶⁾; normalized at irradiation times $t_i = 1 \text{ month}$, cooling time = 1 day.

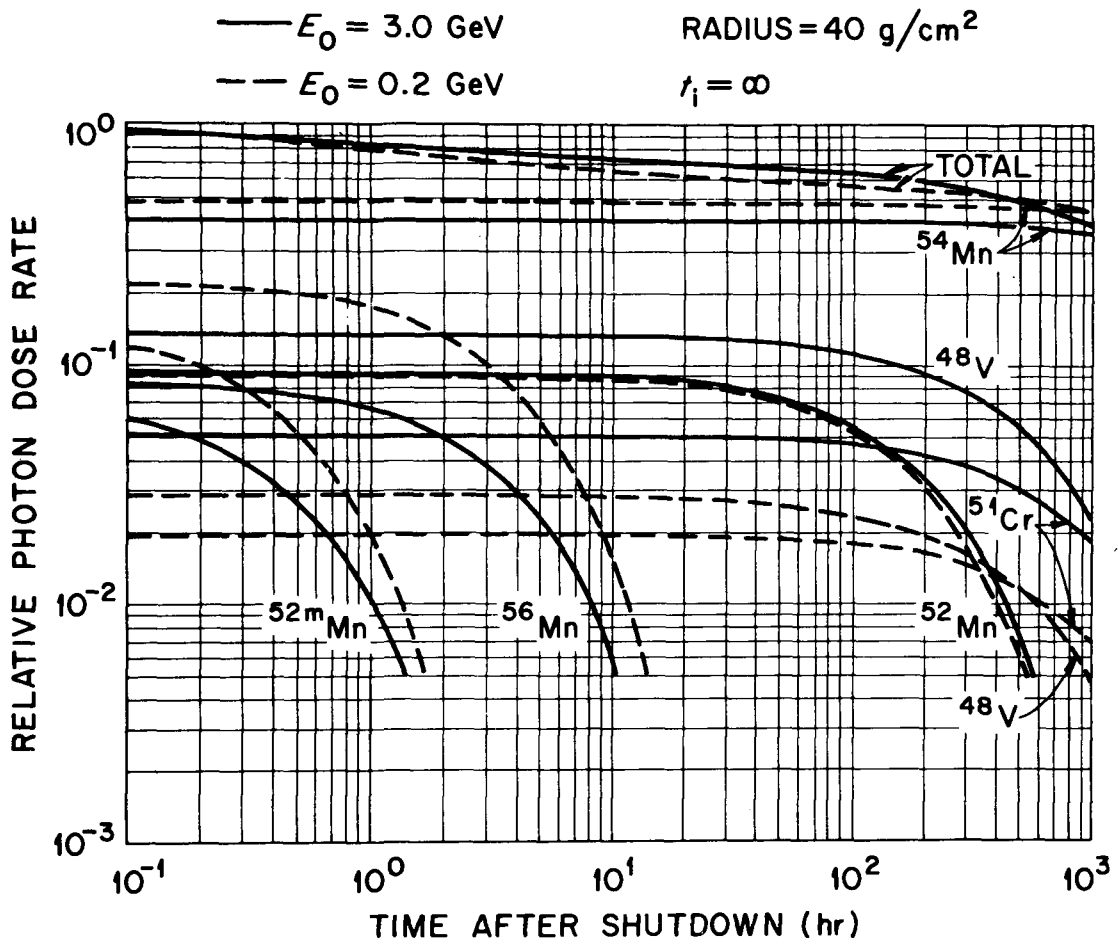


Fig. 27 Relative photon dose-rates at the surface of an iron cylinder versus time after shut-down for infinite irradiation time⁶⁷⁾.

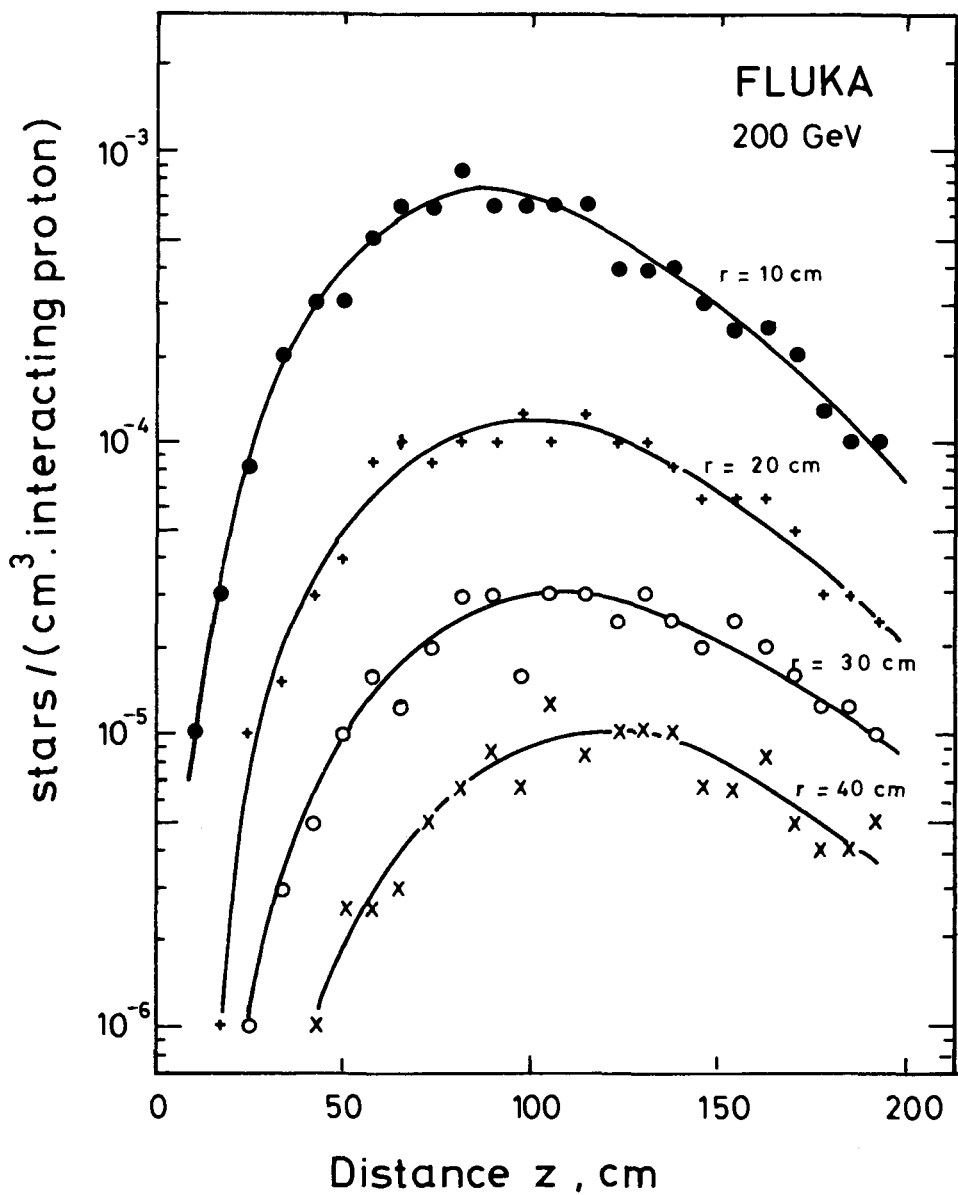


Fig. 28 FLUKA star densities in an iron cylinder⁶⁹⁾.

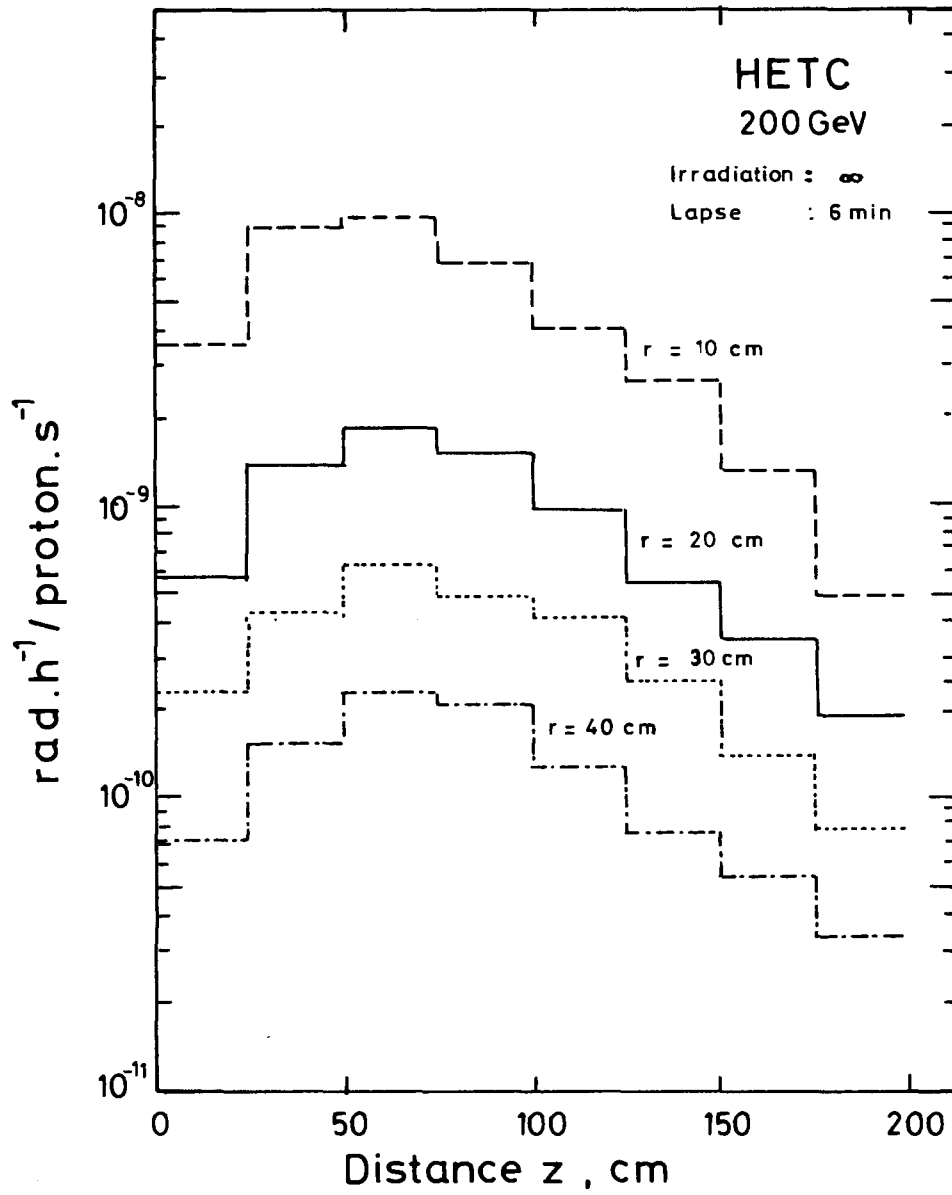


Fig. 29 Remanent photon dose-rates for cylinders of various radii⁶⁹⁾.

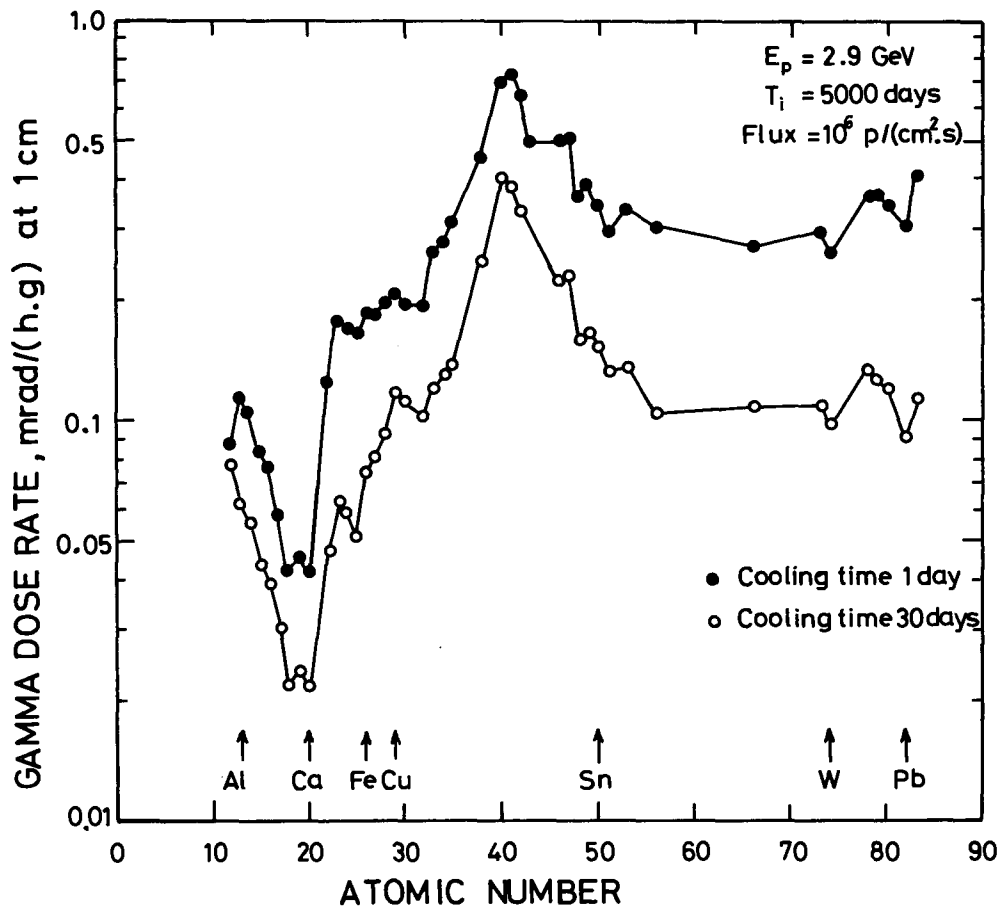


Fig. 30 Variation of remanent gamma dose-rate with atomic number of irradiated element⁶⁵⁾. Data from Ref. 62.